Early Postnatal Dysfunction of mPFC PV Interneurons in Shank3B$^{-/-}$ Mice

Yi-Chun Shih[1,2], Lars Nelson[1,*], Michael Janeček[1,2,*], Michael Matarazzo[1], Rui T. Peixoto[1,2]

1. Department of Psychiatry, University of Pittsburgh, 450 Technology Dr, Pittsburgh, PA 15219, USA
2. Center for Neuroscience at the University of Pittsburgh

* Authors contributed equally

Contact: peixotort@upmc.edu

Rui T. Peixoto is the lead author

Abstract

Medial prefrontal cortex **(mPFC)** dysfunction is associated with cognitive and sensory abnormalities in individuals with autism spectrum disorder **(ASD)**, yet the trajectory of mPFC circuit development in these conditions remains poorly understood. In this study, we investigated the postnatal maturation of glutamatergic connectivity and neuronal excitability in pyramidal neurons **(PYR)** and parvalbumin-positive interneurons **(PVIN)** in the mPFC of mice harboring deletions in SHANK3, a well-established genetic cause of autism associated with severe cognitive impairments and seizures. Our findings reveal early deficits in PVIN excitability that precede changes in the synaptic and intrinsic properties of PYR, resulting in impaired feedforward inhibition. *In vivo* calcium imaging demonstrated hypoactivity of PVIN in dorsal mPFC circuits during early postnatal development, characterized by reduced frequency of calcium transients. By adulthood, excitability phenotypes were reversed, with PVIN becoming hyperexcitable and PYR hypoexcitable. These results suggest that PVIN dysfunction in Shank3B$^{-/-}$ mice emerges during postnatal development and may represent a key pathogenic mechanism and potential therapeutic target in SHANK3-related disorders.

Introduction

Autism spectrum disorders **(ASD)** are marked by significant cognitive deficits that typically emerge during the first years of life [1]. This early symptom onset points to abnormal maturation of medial prefrontal cortex **(mPFC)** as a key factor in ASD pathogenesis [2]. Numerous studies have reported hypertrophy and disrupted functional connectivity in prefrontal cortical regions of autistic children[2–7]. Seizures are highly comorbid with ASD, with many individuals exhibiting preclinical epileptiform activity [8–11], implicating disrupted cortical activity. Studies in mouse models of ASD further corroborate these findings, with many exhibiting abnormalities in mPFC neurons and cortical hyperactivity [12–15]. However, most of studies characterizing mPFC function in mouse models of ASD have focused on adult stages, leaving the early development of these circuits largely unexplored [16]. Despite the critical role of the prefrontal cortex in early cognitive development [17], the specific mechanisms driving the onset of mPFC circuit dysfunction in ASD remain poorly understood.

The prevalence of cortical activity imbalances in autism suggests that deficits in inhibitory mechanisms are a common pathophysiological feature of ASD[18–20]. In particular, changes in GABAergic Parvalbumin **(PV)** interneurons **(PVIN)** have been widely observed in transcriptomic [21,22], and postmortem histological studies of individuals with ASD [23–25]. Many mouse models of autism also exhibit abnormal patterns of PV expression in cortical regions [26–32], as well as disrupted PVIN synaptic connectivity and function [33,34]. Inhibition mediated by PVIN is a critical regulator of cortical circuit activity and synchrony [35,36], and depends on the precise firing of action potentials **(AP)** governed by specialized synaptic and intrinsic properties [37]. Notably, several ASD risk genes disrupt neuronal excitability, glutamatergic synapse development and GABAergic signaling [20,38–40], pointing to a convergence of genetic risk in the postnatal development of PVIN. Given their critical role in mediating cortical inhibition, abnormal PVIN maturation could lead to early imbalances in cortical activity, disrupting key developmental processes that rely on precise neural activity patterns. However, studying the postnatal maturation of PVIN mPFC has been limited by the reliance on PV expression for their identification, as PV is only upregulated in mPFC regions during the third postnatal week [41]. As a result, our understanding of how the early postnatal maturation of PVIN function is altered in mouse models of ASD remains limited.

Mutations in SH3 and Multiple Ankyrin Repeat Domains Protein 3 **(SHANK3)** are one of the most penetrant causes of autism [39,40] and are associated with seizures and profound cognitive impairments [9,42,43]. SHANK3 is a complex gene that encodes a family of postsynaptic scaffolding proteins that regulate the maturation and function of glutamatergic synapses [44]. Deletion of exons Δ13-16 encoding the PDZ domain of SHANK3 in mice **(Shank3B$^{-/-}$)** alters neuronal excitability [45–49] and causes behavioral deficits and hypoconnectivity of mPFC circuits [50–53]. Notably, adult Shank3B$^{-/-}$ mice show

reduced activity of GABAergic interneurons and increased pyramidal neuron **(PYR)** activity in primary somatosensory cortex in response to peripheral sensory stimulation [26,54]. Lower cortical expression of PV is also one of the most replicated findings in Shank3B$^{-/-}$ mice [26,27,32], strongly implicating PVIN dysfunction in these mice. However, since PV expression is activity-dependent [55], it remains unclear whether changes in PV expression observed in adult stages represents a primary pathogenic mechanism or a secondary developmental adaptation.

Here we investigated how the loss of Shank3 disrupts the early postnatal maturation of mPFC circuits by examining the developmental trajectory of glutamatergic synaptic connectivity and membrane excitability in both PYR and PVIN of layer 2/3 **(L2/3)** of anterior cingulate cortex **(ACC)** in Shank3B$^{-/-}$ mice. We focused on the ACC because structural and functional deficits in this prefrontal cortical region are strongly linked to autism [56–59], and reduced ACC PYR activity and synaptic connectivity have been reported in adult Shank3B$^{-/-}$ mice [53]. Our findings reveal that L2/3 ACC PVIN exhibit significant hypoexcitability as early as postnatal day 15 **(P15)**. In addition, PVIN show reduced inhibitory output onto PYR and a substantial reduction in feedforward inhibition **(FFI)** of thalamocortical inputs. At this stage, PYR display normal synaptic and intrinsic properties, suggesting that PVIN dysfunction precedes that of PYR in L2/3 ACC. *In vivo* two-photon calcium imaging further confirmed altered PVIN activity, showing less frequent calcium transients. By adulthood, we observed extensive developmental adaptations in L2/3 ACC circuits, with PVIN becoming hyperexcitable and PYR neurons exhibiting hypoexcitability and a marked reduction in glutamatergic synaptic inputs. These findings suggest that early postnatal PVIN dysfunction is one of the earliest functional phenotypes in L2/3 ACC of Shank3B$^{-/-}$ mice. Additionally, our results highlight the importance of understanding the developmental trajectory of neural circuit maturation in ASD to distinguish between primary deficits and secondary developmental adaptations.

Results

Normal excitability and glutamatergic synaptic inputs of ACC L2/3 PYR in P15 Shank3B$^{-/-}$ mice. Adult Shank3B$^{-/-}$ mice exhibit reduced glutamatergic input in ACC L2/3 PYR [53]. However, many behavioral deficits in these animals already manifest during early postnatal development [60,61], suggesting an early onset of ACC circuit dysfunction. To determine whether loss of Shank3 affects the postnatal maturation of glutamatergic synapses in ACC L2/3 PYR, we recorded AMPAR miniature excitatory postsynaptic currents **(mEPSC)** in acute brain slices of P15 wild-type **(WT)** and Shank3B$^{-/-}$ mice, which provide an estimate of glutamatergic synapse number and strength. Whole-cell recordings in L2/3 PYR were conducted using a cesium-based internal solution in the presence of the voltage-gated sodium channel blocker tetrodotoxin to prevent action potential propagation and evoked synaptic vesicle release, with membrane potential **(V_m)** clamped at -70mV (Fig. 1). We

observed no difference in the amplitude of AMPAR mEPSCs between ACC L2/3 PYR of P15 WT and Shank3B$^{-/-}$ mice (Fig. 1C, average±SD PYR mEPSC amplitude at P15, WT 10.6±1.0pA; KO 10.7±1.3pA, unpaired Mann Whitney **(MW)** test p=0.88. Kolmogorov-Smirnov **(KS)** test p=1.0, n=42,35 neurons from n=4,3 WT and Shank3B$^{-/-}$ mice). In addition, Shank3B$^{-/-}$ PYR showed no difference in average mEPSC frequency compared to WT (Fig. 1D, average±SD PYR mEPSC frequency at P15, WT 2.9±1.8Hz; KO 3.1±1.7Hz, MW test p=0.54. KS test p=0.98), suggesting normal number and strength of glutamatergic synapses at P15. No differences in mEPSC rise and decay times, or membrane capacitance were observed (Supplementary Fig. 1A – 1C and 1E). These findings indicate that the early postnatal maturation of glutamatergic inputs onto ACC L2/3 PYR is largely unaffected by loss of Shank3.

Shank3 deficiency is associated with abnormal neuronal excitability [45–49]. To determine whether the intrinsic properties of ACC L2/3 PYR are altered in *Shank3B*$^{-/-}$ mice during early postnatal development, we performed whole-cell recordings at near physiological temperature in current clamp at P15 with a potassium based internal solution, and measured membrane voltage changes in response to stepped current injections. We detected no difference in AP threshold potential or rheobase current between ACC L2/3 PYR of both genotypes (Fig. 1F and 1G, average±SD PYR AP threshold at P15, WT -34.4±5.5mV; KO -34.2±3.7mV, MW test p=0.9; Rheobase, WT 138.9±39.7pA; KO 141.2±49.7pA, MW test p=0.89, n=25,44 neurons from n=4,5 WT and Shank3B$^{-/-}$ mice), as well as no difference in the relationship between current-voltage **(I-V)** and current-AP firing rate **(I-F)** (Fig. 1H and 1G, two-way ANOVA I-V p=0.22 for genotype. Two-way ANOVA I-F p=0.9 for genotype). Resting membrane potential **(RMP)** and AP kinetic properties were also unaffected (Supplementary Fig. 1F and 1G – 1L), suggesting normal excitability of ACC L2/3 PYR neurons at P15 in Shank3B$^{-/-}$ mice.

Reduced excitability of ACC L2/3 PVIN in P15 Shank3B$^{-/-}$ mice.

GABAergic interneurons in the somatosensory cortex of adult Shank3B$^{-/-}$ mice show reduced responses to peripheral sensory stimulation [54]. In addition, Shank3B$^{-/-}$ mice have abnormal patterns of PV expression throughout cortex [26,27,32]. To determine whether loss of Shank3 alters glutamatergic innervation of ACC PVIN during early postnatal development, we recorded AMPAR-mediated mEPSCs in PVIN of L2/3 ACC of P15 WT and Shank3B$^{-/-}$ mice. To label ACC PVIN during early postnatal development, we injected P7 mice in ACC with AAV9-S5E2-tdTom that expresses tdTomato under control of the E2 enhancer (Fig. 2A and 2E). This approach results in enriched labeling of PVIN [62] which we confirmed through immunohistochemical staining for PV at P21, the developmental stage when PV reaches uniform expression in L2/3 ACC (Supplementary Fig. 2). Approximately 83% of tdTomato-positive (tdTom^{+}) neurons in ACC co-labeled with PV at P21 and 94% in adulthood (Fig.

2B–2D, average±SEM Fraction of S5E2-tdTom$^+$ interneurons with PV$^+$ expression at P21 82.5±1.9%; P60 94.3±4.1%, n=132,125 cells from n=2,3 P21 and P60 mice). This confirms the high specificity of S5E2-based reporters for PVIN [62], and henceforth S5E2$^+$ neurons will be referred to as PVIN in this study. We observed no difference in mEPSC amplitude or frequency in ACC L2/3 PVIN at P15 (Fig. 2G and 2H, average±SD PVIN mEPSC amplitude at P15, WT 20.1±4.1pA; KO 19.8±4.3pA, MW test p=0.54. KS test p=1.0; mEPSC frequency, WT 7.8±3.0Hz; KO 8.4±3.5Hz, MW test p=0.35. KS test p=0.98, n=69,65 neurons from n=5,4 WT and Shank3B$^{-/-}$ mice). There was also no difference in mEPSC rise and decay times or membrane capacitance (Supplementary Fig. 3A – 3C and 2E), suggesting that loss of Shank3 does not impair the early maturation of glutamatergic synapses onto ACC L2/3 PVIN.

To characterize the excitability of PVIN, we performed current-clamp recordings in acute brain slices containing ACC from P15 WT and Shank3B$^{-/-}$ mice. No difference in AP threshold potential and membrane resistance were detected in L2/3 PVIN (Fig. 2J and 2L, average±SD PVIN AP threshold at P15, WT -31.2±3.3mV; KO -31.1±5.0mV, MW test p=0.11. Two-way ANOVA of I-V curve p=0.077 in genotype, n=46,39 neurons from n=5,4 WT and Shank3B$^{-/-}$ mice). However, we observed a significant increase in rheobase current (Fig. 2K, average±SD PVIN rheobase at P15, WT 217.1±75.3pA; KO 254.9±67.0pA, MW test p=0.02) and a rightwards shift in the I-F curve, indicating reduced excitability of L2/3 PVIN at this early postnatal stage (Fig. 2M, two-way ANOVA of I-F curve p=3.3e-8 in genotype). Despite reduced rate of AP firing, no changes in RMP or AP kinetics were observed between genotypes (Supplementary Fig. 3F and 3G – 3L).

Loss of Shank3 reduces MD-ACC feedforward inhibition onto L2/3 PYR at P15.

PVIN are critical regulators of local circuit activity by inhibiting neighboring PYR [35,36]. To determine whether loss of Shank3 impairs the postnatal maturation of PVIN-dependent inhibition in ACC L2/3 circuits, we compared optogenetically evoked PVIN inhibitory postsynaptic currents (oIPSCs) in L2/3 PYR of P15 WT and Shank3B$^{-/-}$ mice. Mice were injected at P7 with AAV9-S5E2-C1V1-YFP in ACC to express the red-shifted excitatory opsin C1V1 in PVIN (Fig. 3A) and acute brain slices containing ACC were used for whole cell-recordings. GABA mediated currents were isolated by performing voltage-clamp recordings at V_m= 0mV in the presence of RS-CPP and NBQX, NMDAR and AMPAR blockers, respectively. oIPSCs were evoked using 1ms 563 nm light pulse to stimulate C1V1 expressing fibers. Notably, the amplitude of oIPSC in Shank3B$^{-/-}$ PYR was reduced two-fold compared to WT, indicating that loss of Shank3 impairs PVIN-mediated (Fig. 3C, average±SD oIPSC amplitude at P15, WT 1.20±0.66nA; KO 0.60±0.60nA, MW test p=2.3e-6, n=72,50 neurons from n=5,4 WT and Shank3B$^{-/-}$ mice). However, no difference in latency to oIPSC peak was detected suggesting normal postsynaptic GABA$_a$ receptor **(GABA$_a$R)** signaling (Fig. 3D, average±SD oIPSC peak time at P15,

WT 14.5±2.7ms; KO 15.1±3.2ms, MW test p=0.46). To rule out potential confounds from variable C1V1 expression levels or viral targeting efficiency, we regressed the YFP intensity in the field of view of the recorded neuron against its oIPSC amplitude. This analysis revealed consistently lower currents in Shank3B$^{-/-}$ pyramidal neurons compared to WT across all fluorescence intensity levels (Supplementary Fig. 4A), indicating that reduced PVIN-dependent oIPSC amplitude in P15 Shank3B$^{-/-}$ ACC is not caused by reduced opsin expression.

PYR and PVIN in L2/3 of the ACC receive robust glutamatergic inputs from the mediodorsal thalamus (MD), with MD-derived inputs selectively driving PVIN-dependent FFI in this region [63]. We recorded MD-driven optogenetically induced excitatory postsynaptic currents (oEPSCs) and FFI oIPSCs onto L2/3 PYR in ACC of P15 WT and Shank3B$^{-/-}$ mice. To stimulate MD fibers in ACC, mice were injected AAV8-hSyn-ChR2-mCherry in MD at P7 (Fig. 3E and 3F). Voltage-clamp recordings in L2/3 PYR were performed in ACSF with RS-CPP, using a low chloride Cs^+ based internal solution with E_{Cl}= -70mV. AMPAR and $GABA_aR$ mediated currents were isolated by holding the recorded neuron at V_m= -70mV and 0mV, respectively. Interestingly, we observed a significant reduction in MD-driven $GABA_aR$ oIPSC amplitude, while AMPAR oEPSC amplitude remained unchanged (Fig. 3H and 3I, average ±SD AMPA oEPSC amplitude at P15, WT 581.8±391.8 pA; KO 505.8±409.3 pA, MW test p=0.4. Average±SD GABA oIPSC amplitude at P15, WT 2.07±0.88 nA; KO 1.39±0.78 nA, MW test p=0.007, n=32,35 neurons from n=4,4 WT and Shank3B$^{-/-}$ mice), resulting in an elevated ratio of excitation/inhibition (E/I) in Shank3B$^{-/-}$ L2/3 PYR when compared to WT (Fig. 3J, average±SD oEPSC/oIPSC amplitude at P15, WT 0.3±0.1; KO 0.4±0.2, MW test p=0.03). Taken together, these results indicate that PVIN-dependent inhibition onto L2/3 PYR in the ACC is markedly reduced by the loss of Shank3 as early as P15.

Reduced glutamatergic synaptic input and excitability of ACC L2/3 PYR in adult Shank3B$^{-/-}$ mice.

To investigate late-stage adaptations in excitatory synaptic function and neuronal excitability, we characterized AMPAR-mediated mEPSCs and the excitability of L2/3 PYR neurons in adult Shank3B$^{-/-}$ mice (Fig. 4A-B). ACC L2/3 PYR displayed lower mEPSC amplitude, consistent to previous reports [53] (Fig. 4C, average±SD PYR mEPSC amplitude at P60, WT 11.4±2.4pA; KO 10.1±1.7pA, MW test p=0.04. KS test p=0.002, n=26,25 neurons from n=3,3 WT and Shank3B$^{-/-}$ mice), but we observed no difference in mEPSC frequency (Fig. 4D, average ±SD PYR mEPSC frequency at P60, WT 1.7±0.7 Hz; KO 2.3±1.3 Hz, MW test p=0.22. KS test p=0.07). In addition, adult Shank3B$^{-/-}$ mice displayed longer mEPSC rise time and slower mEPSC rise velocity of L2/3 PYR in ACC (Fig. 4E and 4F, average±SD PYR mEPSC rise time, WT 1.7±0.2ms; KO 1.9±0.3 ms, MW test p=0.01. Average ±SD

PYR mEPSC rise velocity, WT 9.2±1.7 pA/ms; KO 7.7±1.4 pA/ms, MW test p=0.003), suggesting slower neurotransmission potentially due to abnormal synaptic structural coupling or AMPAR localization. mEPSC decay tau and membrane capacitance were, however, unaffected, suggesting these changes are not due to major changes in AMPAR conductance or cell size (Supplementary Fig. 5A – 5C and 5E).

Next, we examined the cell intrinsic properties of L2/3 PYR in adult ACC by current-clamp recordings. No difference in AP threshold potential, rheobase current or membrane resistance were observed between genotypes (Fig. 4F – 4H, average±SD PYR threshold at P60, WT -35.9±2.9 mV; KO -35.1±2.9 mV, MW test p=0.37. average±SD PYR rheobase at P60, WT 82.1±30.4 pA; KO 90.8±36.4 pA, MW test p=0.54. Two-way ANOVA of I-V curve p=0.35 in genotype, n=24,16 neurons from n=3,2 WT and Shank3B$^{-/-}$ mice). However, we observed a significant reduction in the I-F relationship, indicating hypoexcitability of ACC L2/3 PYR in adult Shank3B$^{-/-}$ mice (Fig. 4M, two-way ANOVA of I-F curve p=3.2e-24 in genotype). Conversely, no difference in RMP and AP kinetics were found, suggesting normal AP generation (Supplementary fig. 5F and 5G – 5L), although the afterhyperpolarization duration was decreased, suggesting changes in potassium or HCN channel conductance in adult Shank3B$^{-/-}$ PYR (Fig. 4L and 4M, average±SD PYR AHP amplitude at P60, WT -45.0±3.1 mV; KO -42.3±4.2 mV, MW test p=0.06. average ±SD PYR AHP duration at P60, WT 502.4±76.4 ms; KO 444.7±38.7 ms, MW test p=0.008). These results indicate that loss of Shank3 results in long-term adaptations of prefrontal circuits, leading to a reduction of AMPAR synaptic strength and hypoexcitability of ACC L2/3 PYR in adulthood.

Late-stage adaptations in glutamatergic synaptic input and intrinsic excitability in L2/3 ACC PVIN of adult Shank3B$^{-/-}$ mice.

GABAergic interneurons of the primary somatosensory cortex of adult Shank3B$^{-/-}$ mice show dampened responses to peripheral stimulation [54], but whether PVIN inhibition is specifically affected remains unknown. Given the excitability deficits observed in ACC L2/3 PVIN at P15 (Fig. 2), we assessed whether the loss of Shank3 leads to permanent PVIN functional deficits in adulthood. To investigate this, we first characterized AMPAR-dependent mEPSCs in ACC L2/3 PVIN of mice injected with AAV5-S5E2-tdTom two weeks prior to the recordings (Fig. 5A-B). Interestingly, we observed a significant reduction of both mEPSC amplitude and frequency in PVIN of adult Shank3B$^{-/-}$ mice when compared to WT controls (Fig. 5C, average±SD PVIN mEPSC amplitude at P60, WT 14.6±2.6 pA; KO 12.9±2.3 pA, MW test p=0.01. KS test p=0.007. Average ±SD PVIN mEPSC frequency at P60, WT 6.3±2.9 Hz; KO 4.5±1.8 Hz, MW test p=0.004. KS test p=0.009, n=31,29 neurons from n=5,4 WT and Shank3B$^{-/-}$ mice). No difference in mEPSC rise and decay times, or membrane capacitance were found, but mEPSC rise velocity was increased (Supplementary fig. 6A

– 6C and 6E). Together, these results suggest reduced number and strength of glutamatergic synaptic inputs onto ACC L2/3 PVIN in adult Shank3B$^{-/-}$ mice.

To determine whether the deficits in neuronal excitability observed at P15 (Fig. 2 and 3) are maintained in adulthood, we characterized PVIN intrinsic excitability and AP firing properties at P60. Surprisingly, and contrary to what we observed during postnatal development, no change in AP threshold potential, rheobase current, or membrane resistance were detected in ACC L2/3 PVIN in adult Shank3B$^{-/-}$ mice (Fig. 5F – 5H, average±SD PVIN threshold at P60, WT -36.3± 5.6mV; KO -38.4±3.7 mV, MW test p=0.46. Average±SD PVIN rheobase at P60, WT 296.7±96.1 pA; KO 279.6±112.8 pA, MW test p=0.56. Two-way ANOVA of I-V curve p=0.28 in genotype, n= 25,24 neurons from n=3,3 WT and Shank3B$^{-/-}$ mice). No change of resting membrane potential and AP properties were also found (Supplementary fig. 6F – 6J). However, PVIN displayed increased AP firing in response to current injections, which is opposite to the phenotype observed at P15 (Fig. 5I, two-way ANOVA of I-V curve p=0.003 in genotype). Likewise, ACC L2/3 PYR of Shank3B$^{-/-}$ mice showed no differences in PVIN-dependent oIPSC amplitude or peak time (Fig. 5L-M and Supplementary Fig. 4B, average±SD oIPSC amplitude at P60, WT 1.00±0.56 nA; KO 1.09±0.56 nA, MW test p=0.54. Average±SD oIPSC peak time at P60, WT 17.7±6.4 ms; KO 15.5±4.1 ms, MW test p=0.14, n=23,25 neurons from n=4,4 WT and Shank3B$^{-/-}$ mice). These results reveal complex developmental trajectories of PVIN synaptic and intrinsic phenotypes and suggest the presence of extensive compensatory mechanisms in PVIN function and inhibition throughout development.

Reduced frequency of Ca^{2+} transients in ACC PVIN of P15-P17 Shank3B$^{-/-}$ mice.

To test whether the excitability and connectivity deficits observed in ACC PVIN at P15 (Fig. 2 and 3) are related to abnormal patterns of cortical activity, we measured spontaneous neuronal activity in ACC of awake WT and Shank3B$^{-/-}$ mice at P15-P17 by *in vivo* two-photon calcium imaging. Mice were co-injected at P7 with AAV9-Syn-GCaMP8s and AAV5-S5E2-tdTom to express GCaMP8s in all cortical neurons and tdTomato in PVIN for labeling (Fig. 6A and 6B). Mice were implanted with a cranial window at P15-P17 and imaged in the same day. Spike-related calcium **(Ca^{2+})** fluorescence of GCaMP8s expressing neurons was recorded at 15Hz frame rate with 920nm excitation light and analyzed using Suite2P [64]. Regions of interest **(ROI)** from PVIN were identified based on tdTomato expression using CellPose [65]. GCaMP8s activity traces from the majority of putative PYR (S5E2-tdTom negative) was characterized by discrete and sparse Ca^{2+} transients, while those from putative PVIN (S5E2-Tom positive) exhibited high frequency, low amplitude transients (Fig. 6C), consistent with the high firing rates and burst firing of cortical PVIN *in vivo* [66]. To compare Ca^{2+} transient properties across animals we calculated ΔF/F and detected Ca^{2+} events using peak finding functions (see Methods). There was no significant genotype differences in the average frequency or amplitude

of Ca^{2+} events in PYR, suggesting normal activity patterns of ACC L2/3 PYR at P16 (Fig. 6D and 6E, average±SD PYR event frequency, WT 0.20±0.2Hz; KO 0.19±0.03Hz, MW test p=0.13, KS test p=0.03; event amplitude, WT 1.45±0.09; KO 1.42±0.13, MW test p=0.60, KS test p=0.97, n=10,9 WT and Shank3B$^{-/-}$ mice). In contrast, changes in PVIN Ca^{2+} activity were more pronounced, showing a significant reduction in event frequency but no difference in event amplitude (Fig. 6G and 6H, average±SD PVIN event frequency, WT 0.20±0.2Hz; KO 0.19±0.03Hz, MW test p=0.04, KS test p=0.02; event amplitude, WT 0.97±0.08; KO 0.99±0.07, MW test p=0.65, KS test p=0.61). We also calculated the area under the curve **(AUC)** of individual Ca^{2+} events and found no difference in AUC of both putative PYR and PVIN in ACC of P16 Shank3B$^{-/-}$ mice (Fig. 6F and 6I, average±SD PYR event AUC, WT 17.4±2.4; KO 18.3±2.5, MW test p=0.39, KS test p=0.76; PVIN event AUC, WT 20.1±4.0; KO 21.6±3.1, MW test p=0.27, KS test p=0.16). Although the average PYR Ca^{2+} event frequency did not show significant differences between genotypes, eCDF analysis of event frequency distribution indicated a trend toward hypoactivity in PYR (Fig. 6D). However, further analysis using deconvolved ΔF/F data to assess event frequency did not support this finding and showed no significant differences in either the mouse averages or the eCDF of deconvolved impulse frequency in PYR (Supplementary fig. 7A). In contrast, deconvolved analysis of PVIN traces confirmed a significant reduction in frequency of Ca^{2+} transients, consistent with lower ACC PVIN activity (Supplementary fig. 7E). No difference in Ca^{2+} transient rise time, duration, and decay tau was detected in both PYR and PVIN between genotypes (Supplementary fig. 7B – 7D and 7F – 7H). Together, these results suggest that loss of Shank3 causes overall hypoactivity of PVIN in ACC during early postnatal development.

Deep layer cortical neurons exhibit one of the highest co-expression rates of ASD risk genes [57] and are functionally impaired in several mouse models of ASD [12,14,15]. To determine whether the deficits in PVIN Ca^{2+} activity are restricted to specific cortical layers we analyzed ROIs segregated by their mediolateral **(ML)** distance to the central sinus corresponding to superficial (100-375 μm) and deep layers (>375 μm). Interestingly, PVIN showed similar trends in event frequency, amplitude, and AUC across the ML axis, suggesting that loss of Shank3 similarly disrupts PVIN activity across cortical layers in dorsal ACC (Fig. 7A – 7C and Supplementary fig. 8, average±SD superficial PVIN event frequency, WT 0.22±0.02 Hz; KO 0.17±0.04 Hz, MW test p=0.01. Average±SD superficial PVIN event amplitude, WT 1.0±0.1; KO 0.9±0.1, MW test p=0.53. Average±SD superficial PVIN event AUC, WT 20.3±5.0; KO 20.1±2.5, MW test p=0.73. Average±SD deep PVIN event frequency, WT 0.23±0.03 Hz; KO 0.19±0.02 Hz, MW test p=0.02. Average±SD deep PVIN event amplitude, WT 1.0±0.1; KO 1.0±0.1, MW test p=0.66. Average±SD deep PVIN event AUC, WT 21.0±4.0; KO 24.3±2.9, MW test p=0.11). To test whether loss of Shank3 alters activity correlation between different cell populations in ACC at P16, we measured Pearson correlation coefficients of deconvolved ΔF/F activity between PYR-PYR, PYR-PVIN, and PVIN-PVIN ROI pairs. We detected a significant reduction in correlation

between all neuronal types with increased cell-cell distance. However, there was no statistical difference in the correlation of Ca^{2+} activity between any cell types across genotypes (Fig. 7D – 7I, PYR-PYR KS test p=0.2. PVIN-PVIN KS test p=1.0. PVIN-PYR KS test p=1.0), suggesting that the correlation of ACC PYR and PVIN activity measured by GCaMP8s imaging is not significantly affected by loss of Shank3.

Discussion

Structural and functional deficits in the mPFC have been consistently reported in children with autism [56–59] but the precise neural mechanisms underlying the onset of prefrontal cortical dysfunction in ASD remain unclear. In this study, we examined the postnatal maturation of PVIN and PYR in L2/3 of the ACC in Shank3B$^{-/-}$ mice, focusing on their excitability, glutamatergic synaptic connectivity, and *in vivo* activity. Our results reveal that deficits in L2/3 PVIN excitability are already observed by P15 (Fig. 2). This finding is important because this developmental stage in mice is analogous to early childhood in humans, when ASD symptoms typically emerge. The reduction in PVIN excitability was accompanied by significant deficits in PVIN-mediated inhibition of PYR, as shown through direct optogenetic stimulation and thalamocortical driven inhibition (Fig. 3). Two-photon calcium imaging further demonstrated overall hypoactivity of PVIN in ACC circuits during early postnatal development, suggesting that the physiological abnormalities detected in PVIN alter their function *in vivo* (Fig. 6). By adulthood, both PVIN and PYR exhibited extensive developmental adaptations, resulting in contrasting phenotypes compared to early postnatal stages (Fig. 4 and 5). These results indicate that the loss of Shank3 causes early dysfunction of mPFC circuits, with deficits in PVIN excitability and PVIN-mediated FFI emerging as one of the earliest physiological abnormalities in the ACC of Shank3B$^{-/-}$ mice during postnatal development.

Deficits in ACC L2/3 PVIN excitability emerge during early postnatal development.

PVIN play a critical role in controlling local cortical circuit activity by providing fast, reliable, and temporally precise inhibition[37,67]. This inhibitory function depends on specialized molecular and cellular mechanisms in PVIN including voltage-gated channels optimized for rapid action potential generation and regeneration [36]. In our study, we observed a significant reduction in the excitability of L2/3 PVIN in the ACC at P15, characterized by an elevated rheobase and reduced firing rates in response to current injections (Fig. 2). Other intrinsic properties, such as resting membrane potential, membrane resistance, AP threshold, and AP kinetics, were unchanged (Supplementary fig. 2), suggesting that the deficits in AP firing might arise from impaired action potential initiation [68]. We also

observed reduced inhibition onto PYR following stimulation of MD thalamocortical afferents. Notably, FFI elicited by MD projections in the ACC is exclusively mediated by PVIN [63] and is essential for maintaining the balance between excitation and inhibition of local cortical circuits [35,36]. Our results demonstrate that the loss of Shank3 disrupts PVIN function and local cortical circuit inhibition during postnatal development. Reduced PVIN-mediated FFI could be due to insufficient excitatory drive onto PVIN, reduced excitability, or deficient postsynaptic GABAergic signaling in PYR. We observed no differences in AMPAR mEPSC frequency or amplitude in L2/3 PVIN at P15, suggesting that number and strength of glutamatergic synapses in PVIN are unaffected at this stage. However, the substantial reduction in oIPSC amplitude in L2/3 PYR driven by optogenetic stimulation of local PVIN (Fig. 3A-3D), and the shifted input-output (I/F) relationship of PVIN (Fig. 2M) suggest that deficits in excitability and AP generation may be the underlying causes of early PVIN dysfunction in Shank3B$^{-/-}$ mice. PVIN undergo extensive postnatal maturation of their intrinsic properties during this postnatal period, suggesting the observed changes could reflect a delayed neuronal maturation [69]. However, because parameters such as resting membrane potential, membrane resistance, and AP kinetics were normal, the alterations in rheobase and I/F relationship likely reflect disruption of specific physiological mechanisms and not a general developmental delay. It remains unclear whether reduced excitability of PVIN is directly caused by loss of Shank3 loss or arises as a consequence of altered network activity. However, given that conditional deletion of Shank3 specifically in interneurons leads to cortical dysfunction and behavioral abnormalities in adulthood, it is possible that this phenotype is driven by cell-autonomous mechanisms [54,70,71]. Future studies identifying the specific mechanisms and signaling pathways disrupted by the loss of Shank3 in PVIN will be crucial for understanding the early pathophysiology of mPFC circuits in Shank3B$^{-/-}$ mice.

Altered *In Vivo* Calcium Dynamics in ACC L2/3 PVIN.

In vivo two-photon calcium imaging of ACC neurons revealed reduced frequency of GCaMP8s calcium transients in PVIN of Shank3B$^{-/-}$ mice during postnatal development (Fig. 6). This reduction was observed across the entire medio-lateral extent of the ACC (Fig. 7), indicating decreased PVIN activity in both superficial and deep cortical layers. Although eCDF analysis of ROI event frequency suggested a trend toward hypoactivity in PYR (Fig. 6D), this was not supported by mouse averages of event frequency or deconvolved impulse frequency analysis of ΔF/F traces (Supplementary fig. 7). In contrast, the deconvolved impulse data showed a significant reduction in Ca^{2+} event frequency in PVIN, but not PYR, consistent with PVIN hypoactivity at P15. No significant differences were observed in the correlation of Ca^{2+} activity between different neuron types, though a trend toward reduced PVIN-PVIN correlation was noted (Fig. 7). This suggests potential deficits in PVIN synchrony that will require methods with higher temporal resolution to address. The reduction in ACC neural activity aligns with previous studies reporting reduced mPFC activity in Shank3B$^{-/-}$ mice [53,72], but contrasts with findings

of hyperactivity in sensorimotor regions of Shank3-deficient mice during both postnatal and adult stages [48,54,73–75]. This discrepancy may arise from differential impacts of Shank3 loss on mPFC versus neocortical circuits due to varying rates of postnatal maturation or different influences of abnormal sensory input, which are perturbed in Shank3B$^{-/-}$ mice [27,31]. The reduction in GCaMP8s signal transients in PVIN is consistent with the excitability deficits we observed in our whole-cell recordings (Fig. 2). It also supports a previous finding that Shank2-deficient mice have reduced burst firing in PVIN [66], suggesting that PVIN dysfunction might be a common pathophysiology of Shankopathies. Notably, Shank3 regulates HCN2 channel expression, and its loss is associated with reduced I_h currents mediated by HCN channels [46,48,68]. In PVIN, HCN2 is predominantly located in the axon and axon hillock, playing a key role in action potential burst generation [68]. Early deficits in HCN2 function could be a cell-autonomous mechanism linking Shank3 deletion with reduced PVIN burst firing. An additional possibility is that the early hypoexcitability of PVIN might arise as a compensatory adaptation to reduced afferent innervation or excitatory drive to mPFC regions. This is supported by reports of reduced functional connectivity in prefrontal regions of adult Shank3 KO mice [52,53], but whether this hypoconnectivity emerges early in development remains unclear. Future studies using region- and developmental stage-specific approaches, alongside electrophysiological techniques with higher temporal resolution, will be essential for elucidating the mechanisms underlying Shank3-related dysregulation of early cortical activity.

Synaptic and Neuronal Adaptations in Adulthood.

A striking finding from our study was the extensive neuronal adaptations observed in adulthood compared to early postnatal development. There was a complete reversal of PVIN excitability, with an increased I/F relationship in response to current injections (Fig. 5I). Glutamatergic inputs onto PVIN were also significantly weakened, as indicated by a pronounced reduction in mEPSC frequency and amplitude (Fig. 5C and 5D). Despite this, we observed normal oIPSC in response to optogenetic stimulation of PVIN onto PYR (Fig. 5N), suggesting that overall PVIN inhibitory drive may be normalized throughout development. We also observed significant changes in the intrinsic and synaptic properties of PYR (Fig. 4). Specifically, PYR excitability was markedly reduced, with a pronounced decrease in the I/F relationship. Additionally, AMPAR mEPSCs exhibited reduced amplitude and slower kinetics, suggesting postsynaptic alterations in AMPAR properties. This depression of AMPAR synapses is consistent with a previous study that reported reductions in both mEPSC frequency and amplitude in ACC L2/3 PYR [53]. However, we did not observe a significant difference in mEPSC frequency, which may be attributed to the higher mEPSC amplitude cutoff (7 pA) we used in our study. Overall, our data show a decrease in excitatory drive onto both PVIN and PYR in L2/3 ACC in adulthood, consistent with reduced ACC glutamatergic connectivity in adults[52]. The bidirectional changes in excitability in PVIN and PYR may represent compensatory adaptations

aimed at counterbalancing network hyperactivity, but further studies will be needed to fully understand how PVIN function is altered in adult cortical circuits. Importantly, these findings demonstrate that the phenotypes observed in adulthood do not reflect the early pathophysiological changes induced by loss of Shank3, highlighting the importance of characterizing early postnatal development in mouse models of ASD. Such early characterization may help identify therapeutic targets that can effectively ameliorate abnormal developmental trajectories of cortical circuits.

Role of Shank3 in the postnatal maturation of mPFC neurons.

Shank3 is widely recognized as a key postsynaptic scaffold protein at glutamatergic synapses[44]. However, our findings indicate that glutamatergic input onto both PYR and PVIN in layer 2/3 of the ACC is largely unaffected by the loss of Shank3 at P15 (Fig. 1 and 2). This suggests that Shank3 is either not essential or can be compensated for during synaptogenesis and early maturation of glutamatergic synapses *in vivo*. In contrast, PVIN excitability is already disrupted at this stage (Fig. 2), suggesting that non-synaptic mechanisms regulated by Shank3 may underlie this phenotype. Several studies have shown that Shank3 plays a crucial role in regulating Ca^{2+} signaling and homeostasis in neurons and muscles [76,77]. In neurons, Shank3 interacts with neuronal L-type voltage-gated Ca^{2+} channels and influences gene expression by regulating intracellular calcium signaling [78,79]. Given the critical role of Ca^{2+} signaling and buffering in PVIN function, PVIN may be particularly vulnerable to abnormal calcium regulation following the loss of Shank3. Our results highlight the non-synaptic role of Shank3 in the maturation of mPFC neurons, suggesting disruption of these mechanisms might have significant pathogenic implications in ASD.

Implications for ASD research.

Individuals with SHANK3-related disorders often develop seizures and exhibit patterns of epileptiform activity [9,42,80]. Our findings of early PVIN dysfunction, followed by more pronounced synaptic deficits in adulthood, suggest that early targeting of PVIN excitability may be a promising therapeutic avenue for preventing the onset of cortical activity imbalances in SHANK3-related disorders. Enhancing GABAergic function has shown potential in correcting abnormal behaviors in mouse models of ASD [81,82]. More recently, modulating PVIN excitability through PVIN-enriched Kv3 channels has yielded promising results in improving behavioral abnormalities in mouse models of Fragile X syndrome [83,84]. Our study provides new insights into the developmental trajectory of PVIN and PYR neuron dysfunction in the mPFC of Shank3B$^{-/-}$ mice and reinforce the notion that early PVIN dysfunction is a key driver of cortical activity imbalances in ASD.

Acknowledgements

We thank Andrew D'Agostino, Tasha Merchant, Lan Chen and Sidney Dawkins for assistance with mouse husbandry and genotyping. We thank Susana Silva, David Lewis, Gary Thomas and Stephanie Rudolph for helpful comments on the manuscript. R.T.P. was supported by R01MH124695, R21MH132015 and a Bridge to Independent Award from the Simons Foundation Autism Research Initiative. L.N. was supported by T32MH16804.

Author Contributions

R.T.P. conceived and designed the study. Y-C.S., L.N., and M.J. performed electrophysiological experiments, and Y-C.S. analyzed the electrophysiological data. Y-C.S. collected and analyzed the two-photon microscopy data. M.M. performed immunohistochemistry. L.N. developed scripts for electrophysiological data analysis, and Y-C.S. and R.T.P. developed scripts for two-photon data analysis. Y-C.S. and R.T.P. wrote the manuscript with input from all other authors.

Methods

Animals

All experimental manipulations on mice were performed in accordance with protocols approved by the Institutional Animal Use and Care Committee at the University of Pittsburgh in compliance with the guidelines described in the US National Institutes of Health *Guide for the Care and Use of Laboratory Animals*. Mice were housed on a 12/12hr light/dark cycle with chow and water provided ad libitum. Mice were weaned at P21-23 and separated by sex in cages of 2-5 animals of mixed genotypes. Shank3B$^{-/-}$ mutant mice were described previously[61] and obtained from The Jackson Laboratory (#017688). Characterization of neural properties by electrophysiology was performed in Shank3B$^{+/+}$ and Shank3B$^{-/-}$ age-matched mice from breeding pairs between Shank3B$^{+/-}$ heterozygous animals. Male mice were used in all experiments.

Viruses and stereotaxic intracranial injections

Intracranial viral injections were performed at P7-P8 (for experiments performed at P15) or 2 weeks before experiments (for experiments performed in adult mice). Mice were anesthetized with isoflurane (4% for induction and 1-2% thereafter for maintenance) and placed into a stereotaxic apparatus (Kopf Instruments model 1900). The hair around the site of incision was removed by hair removal creams (Nair). The surgical area was cleaned by 2% iodine and 70% alcohol solution. To perform intracranial injections, injection sites were poked by sterile 30G needle in P7 pups and drilled by Micromotor drill (Stoelting) in adults, respectively. All skull measurements were made relative to Bregma, and AAV solutions were delivered by injecting 350 nl at a maximum rate of 75 nL/min using a Harvard

Apparatus PHD ULTRA CP injector. For labeling of ACC PVIN, an adenoassociated virus (AAV) expressing tdTomato under the PVIN specific S5E2 enhancer (AAV9-S5E2-tdTomato, Addgene 135630-AAV9) was injected in mice using coordinates: AP +0.5 mm; ML 0.3 mm; Depth -1.0 mm for P7 pups and AP +1.1 mm; ML 0.35 mm; Depth -1.1 mm for adults. AAV9-S5E2-C1V1-YFP (Addgene 135633-AAV9) was used for expressing the red-shifted channelrhodopsin C1V1 in PVIN. Co-expression of GCaMP8s and S5E2-tdTom in ACC for two-photon imaging experiments was achieved by injecting AAV-syn-jGCaMP8s-WPRE (Addgene 162374-AAV9) and AAV9-S5E2-tdTomato at a 2:1 ratio. AAV-hChR2(H134R)-mCherry (Addgene 26976-AAV8) was used for expressing ChR2 in MD with coordinates: AP -0.9 mm; ML 0.4 mm; Depth -3.2 mm for P7 pups. Mice received carprofen (5 mg/kg) for analgesia before surgery. Following injections and wound suture, mice were placed on heating pad until being fully awake and returned to home cages for at least 7 days.

Brain slice preparation and whole-cell electrophysiology

Acute brain slices were prepared following anesthesia by isoflurane inhalation and transcardiac perfusion with ice-cold artificial cerebrospinal fluid (ACSF) containing (in mM): 125 NaCl, 2.5 KCl, 25 $NaHCO_3$, 2 $CaCl_2$, 1 $MgCl_2$, 1.25 NaH_2PO_4 and 25 glucose (310 mOsm per kg). Cerebral hemispheres were removed and transferred into a slicing chamber containing ice-cold ACSF. Coronal slices including ACC (275 μm thick) were cut with a Leica VT1200s vibratome and transferred for 10 min to a holding chamber containing choline-based solution consisting of (in mM): 110 choline chloride, 25 $NaHCO_3$, 2.5 KCl, 7 $MgCl_2$, 0.5 $CaCl_2$, 1.25 NaH_2PO_4, 25 glucose, 11.6 ascorbic acid, and 3.1 pyruvic acid at 33°C. Slices were subsequently transferred to a chamber with pre-warmed ACSF (33°C) and gradually cooled down to room temperature (20–22°C). All recordings were obtained within 4 hours of slicing. Both ACSF and choline solution were constantly bubbled with 95% O_2 and 5% CO_2. Individual slices were transferred to a recording chamber mounted on an upright microscope (Olympus BX51WI) and continuously perfused (1–2 ml per minute) with ACSF at room temperature. Cells were visualized using a 40× water-immersion objective with infrared illumination. Whole-cell voltage clamp recordings were made from PYR or PVIN of ACC. Patch pipettes (2.5–4 MΩ) pulled from borosilicate glass (BF150-86-7.5, Sutter Instruments) were filled with a Cs^+-based internal solution containing (in mM): 130 $CsMeSO_4$, 10 HEPES, 1.8 $MgCl_2$, 4 Na_2ATP, 0.3 NaGTP, and 8 Na_2-phosphocreatine,10 $CsCl_2$, 3.3 QX-314 (Cl^- salt), (pH 7.3 adjusted with CsOH; 300 mOsm per kg) for voltage-clamp recordings. Alexa Fluor 488 dye (0.07%) was added to the internal solution to fill the patched cell and examine dendritic morphology. PYR identity was validated by the presence of an apical dendrite and spiny dendrites, whereas PVIN were identified by S5E2-Tom expression and validated by aspiny dendritic morphology. For all voltage-clamp experiments, errors due to voltage drop across the series resistance (<20 MΩ) were left uncompensated. For mEPSC recordings, ACSF contained 1 μM TTX, 1 μM (RS)-CPP, and 1 μM Gabazine, and recordings were performed at room

temperature (20-22˚C) with V_m = -70 mV. After breaking in, cells were left to stabilize for 4 min and currents were then acquired continuously for 5 min. Membrane currents and potentials were amplified and low-pass filtered at 3 kHz using Multiclamp 700B amplifier (Molecular Devices), digitized at 10 kHz, and acquired using National Instruments acquisition boards and a custom version of ScanImage written in MATLAB (Mathworks). Calculation of input resistance and membrane capacitance in voltage clamp recordings was performed by fitting evoked currents in response to -5 mV voltage steps in the first seconds after cell break-in. For current-clamp recordings, potassium-based internal solution containing (in mM): 130 $KMeSO_3$, 10 HEPES, 3 KCl, 1 EGTA, 4 Na_2ATP, 0.3 NaGTP, and 8 Na_2-phosphocreatine, (pH 7.3 adjusted with CsOH; 300 mOsm per kg) was used. No drug was added to the bath, and recordings were performed at 31-33˚C. Cell was broken in with V_m = -70 mV and allowed to stabilize for 4 min in voltage-clamp. After stabilization, resting membrane potential was measured at I = 0. Current-clamp recording was performed by adjusting holding current to maintain the V_m at -70mV. Four cycles of 700ms current steps -100 pA to 350 pA in 25 pA increments were injected and V_m changes recorded and averaged. For oIPSC recordings, voltage-clamp was performed in Cs^+-based internal solution for measuring optogenetically evoked synaptic currents. Cells were held at V_m = 0 mV in ACSF with 1 μM (RS)-CPP and 1 μM NBQX. C1V1-dependent oIPSC was induced by a 1ms 5.5mW 563nm light pulse (CoolLED pE-300) delivered through the objective. For controlling fiber density, YFP fluorescence in the field of view was imaged with 10.2 mW 473nm light for 100ms, centering on patched cell. For recordings of MD-driven feedforward inhibition, 1 μM (RS)-CPP was added to ACSF, and a modified low-chloride Cs^+-based internal solution containing (in mM): 130 $CsMeSO_4$, 10 HEPES, 1 EGTA, 4 Na_2ATP, 0.3 NaGTP, and 8 Na_2-phosphocreatine, 3.3 QX-314 (Cl^- salt) was used. Cells were held at -70 mV and 0 mV for measuring AMPA and GABA currents, respectively. ChR2-dependent oEPSC was induced by 1ms 7mW 473nm light pulse. mCherry intensity in the field of view was captured with 5.5mW 563nm LED for 100ms. Electrophysiology recordings were performed in a custom version of ScanImage and saved as Matlab files for subsequent off-line analysis using the custom Python program ClampSuite (available at github.com/LarsHenrikNelson/ClampSuite).

Brain tissue imaging and immunohistochemistry

Mice were deeply anesthetized with isofluorane and perfused transcardially with 1X phosphate-buffered saline (PBS) (pH 7.4) followed by 4% paraformaldehyde in PBS. Brains were fixed overnight at 4°C, washed in phosphate buffer saline (PBS) and sectioned (50 μm) coronally using a vibratome (Leica VT1000s). For immunohistochemistry, brain sections were incubated in blocking buffer containing: 10% normal goat serum, mouse IgG (1 μg/mL) and 0.3% triton X-100 in 1X PBS for one hour at room temperature. After blocking, sections were incubated overnight with anti-Parvalbumin

antibodies (1:10000, SWant PV235) and anti-VVA biotinylated antibodies (1:400, Vector Laboratories) at 4°C. After the sections were washed, they were incubated with anti-mouse Alexa 488 (1:2000, Jackson ImmunoResearch) or Alexa 647 (1:2000, Abcam), Streptavidin-Alexa 594 (1:2000, Jackson ImmunoResearch), and DAPI (1 µg/mL, Thermo Fisher) for 1-2 hours at room temperature. The sections were mounted on glass slides, dried and mounted with ProLong antifade reagent containing DAPI (Molecular Probes). Whole brain sections were imaged using and Olympus VS200 slide scanner with 10X and 40X objective lens. For quantification of PV-tdTom co-localization slices were imaged in an Olympus FV1200 confocal microscope with 60X objective lens. Three slices containing ACC were analyzed per animal to quantify percentage of PV-positive cells among S5E2-tdTom labeled population. For each slice three regions of L2/3 were randomly selected and imaged, and cell number was manually quantified. PV signal was analyzed in ImageJ and considered positive if fluorescence intensity was 2.5x above the background. A population of S5E2-tdTom-labeled cells with very small cell size (<100 μm^2) in adult ACC was excluded from quantification and whole-cell patch clamp recordings.

Cranial window implants

P15-P17 mice previously co-injected with AAV-GCaMP8s and AAV-S5E2-tdTom were anesthetized with isoflurane as previous described. Mice received carprofen for analgesia before surgery. Eye ointment (Systane) was applied to prevent eyes dry during the surgery. The hair on scalp was removed using the hair removal cream (Nair) and the surgical area further cleaned by 2% iodine and 70% ethanol solution. The scalp over the surgical area was removed and the skull was cleaned again with 2% iodine and 70% ethanol solution. The skull above the injection site was carefully drilled using a micromotor drill to open a craniotomy of approximately 3.5 mm diameter. The drilling site was rinsed with ice-cold sterile saline after every round of drilling. Ice-cold 0.01% epinephrine solution (Fisher scientific) was injected under the skull, and bone fragments were carefully removed with sharp forceps. The dura was kept intact and moist with sterile saline. Exposed area of the brain was routinely rinsed with ice-cold epinephrine solution until no bleeding was observed. Pre-sterilized 5 mm diameter coverslips (Thermofisher) were then gently placed on the brain surface with sterile saline added between the coverslip and the brain. The edges of the coverslip were glued to the skull using LOCTITE 454 superglue, and a custom titanium headpost was subsequently secured using Metabond cement (C&B Metabond). Following surgery, mice were placed on a heating pad until awakening. Grated rimadyl (Bio-Serv, 2 mg/tb) mixed with RO water was provided during recovery time before recordings (>2 hours).

Two-photon calcium imaging

Two hours following recovery from window implantation, mice were head-fixed on top of a heating pad (37˚C) in a custom stage with goniometers for fine tilt adjustments. Images were acquired using

a resonant scanning two-photon microscope (Ultima 2P plus, Bruker, WI) at 15 Hz frame rate and 512x512 pixel resolution through a 16x water immersion lens (Nikon 16x 0.8NA). Dorsal ACC was imaged at a depth between 150 and 350 μm in dorsal ACC regions with GCaMP8s and S5E2-tdTom expression. Excitation light (920 nm/1100nm wavelength) was provided by a tunable femtosecond infrared laser (Insight X3, Spectra-Physics, CA). Tunable wavelength beams were combined with a dichroic mirror (ZT1040dcrb-UF3, Chroma, VT) before being routed to the microscope's galvanometers. PrairieView software (vX5.5 Bruker, WI) was used to control the microscope. Multiple 6 min imaging sessions were acquired from each mouse at varying depths. After each imaging session, 20 μm z-stacks with 5 μm spacing were imaged with 1100 nm excitation for S5E2-tdTom visualization. Mediolateral distance of the field of view was measured in relation to the central sinus to estimate cortical layer.

Two-photon calcium imaging data analysis

Sequential images of GCaMP8s fluorescence were registered and motion corrected in Suite2p (v0.10.3, Cellpose v0.7.3). Regions of interest (ROIs) were identified based on functional segmentation by correlating pixel intensity across time. Z-stack images of S5E2-tdTom fluorescence were collected using 1100 nm laser excitation and projected into a single plane using ImageJ, with S5E2-tdTom positive cells identified using CellPose (Strubger et al. 2021). For each recording, we collected 5380 images at ~15 Hz frame rate. Data was further processed using a custom Python script for movement artifact removal, signal deconvolution, and Ca^{2+} transient quantification (Lab Github). Movement artifacts were identified by calculating the spatial displacement of the imaging plane across frames using the vectorized xoff/yoff shift from the Suite2p ops.npy file. Image segments with frame-to-frame shifts exceeding a threshold of 1.5 were removed and surrounding frames were concatenated and smoothed using a Savitzky-Golay filter (window size of 15 frames, polynomial order of 3). Fluorescence traces were corrected for neuropil contamination by subtracting a scaled version of the neuropil signal (F_subt = F - 0.7 * Fneu). Baseline fluorescence (F0) was estimated using a rolling 8th percentile function over a 120-second window [107]. The normalized change in fluorescence (ΔF/F) was calculated as ΔF/F = (F − F0) / F0. For Ca^{2+} event quantification, we detected peaks in the filtered ΔF/F trace using the SciPy findpeaks function with the following parameters: [PYR: distance = 3, prominence =0.5, width = 3; PVIN: distance = 2, prominence =0.4, width = 1]. Event amplitude, frequency, area under the curve (AUC), rise time, tau, and duration were calculated to quantify calcium event properties. To account for phase shifts introduced by wavelet filtering, each detected peak position was redefined by searching for the local maximum in the unfiltered ΔF/F trace within 3 frames around the identified peak. To determine the onset (and thereby the baseline) of an event, we first identified the minimum ΔF/F value in the 20 frames preceding the event peak (equivalent to 1.33 seconds at 15 Hz). For events with ΔF/F values below 1.5, we reduced the search window to 15 frames. From this minimum, we considered all indices where ΔF/F values were less

than the minimum + 0.15. We then calculated the slopes from these points to the event peak, identifying potential onset indices as those with a slope greater than max slope - 0.03. Among these candidates, we selected the index closest to the peak as the true event onset. Event amplitude was calculated as the ΔF/F value at peak minus the value at peak onset. The end of the event was defined as the point at which ΔF/F reached 37% of peak amplitude, or the onset of the next peak, whichever happened first. Area under the curve (AUC) was measured by integrating the values from the event onset to event end. ROIs were excluded based on the following criteria: [all event parameters (frequency, amplitude, etc) = 0, noise size > 1, F < 80, and F_subt < 40]. For activity correlation analysis, we used deconvolved data to avoid overestimation of correlation between ROI. Fluorescence traces were deconvolved using the OASIS AR(1) model with FOOPSI to extract spike rates, representing underlying neural activity. Only deconvolved events with amplitudes exceeding 0.05 were retained for further analysis. Deconvolved traces were then smoothed using a 300 ms moving average and further used to compute the correlation between neural activity and the spatial distance between cells. For this, we calculated pairwise Pearson correlations and Euclidean distances between all ROIs and generated correlation matrices and distance matrices. The averaged cumulative distribution of Pearson correlations was measured by averaging cumulative distribution of all ROIs of each individual animal. These analyses were performed separately for both PYR and PVIN cell populations.

Electrophysiology data analysis

mEPSCs, current-clamp, and oEPSC/oIPSC were analyzed using a custom python-based program Clampsuite available at https://github.com/LarsHenrikNelson/ClampSuite. Acquisitions had the mean removed and were filtered using a zero-phase Remez filter with a low pass filter at 600 Hz and 600 Hz wide. Events were identified using a modified FFT deconvolution method similar to Pernia-Andrade et. al. 2012. Events were discarded based on the following criteria: Events smaller than 7 pA (measured from the baseline to the peak), a rise time faster than 0.5 ms, a rise time (time from baseline to event peak) slower than the decay, a rise time slower than 4 ms, a minimum decay time of 0.5 ms and a minimum interevent distance of 1 ms. Tau was estimated using the following equation: (event amplitude) * (1 / exp(1)) and the time when the event reached tau was interpolated from the time data. Rise time was calculated as the time from the start of the mEPSC/IPSC to the peak. Rise rate is the amplitude of the mEPSC/IPSC divided by the rise time. Occasionally an event was manually removed or labeled. For oEPSC/oIPSC analysis, oEPSC peak was identified in the 5-20 ms poststimulation window, and oIPSC peak was identified 5-50 ms after stimulation. For analysis of current clamp recordings evoked potentials were analyzed ClampSuite. All spike statistics, except spike rate, were calculated from the first acquisition of each cycle (ranging from –100 to 300 pA in order from most negative to most positive) that contained at least one spike and taking the mean of

the values of all APs in the cycle. The following were calculated from the first spike of each acquisition containing a spike: spike threshold, peak spike velocity, start of the AHP, spike width, spike peak voltage, and spike duration. The spike threshold was identified using the third derivative method. The peak spike velocity was the peak of the first derivative of the spike. The start of the AHP was calculated from the third derivative of the spike. The spike peak voltage was calculated as the maximum voltage of a spike. The membrane resistance was calculated from the first 7 pulses (-100 to 50 pA) by regressing the ΔV (y) against the pulse amplitude (x) and taking the slope as the membrane resistance. Vm was calculated as the mode of the moving average during the step duration. The spike frequency (Hz) of each pulse step was the average number of spikes divided by the time of each pulse step. Acquisitions without spikes were assigned a null value and did not count towards the mean Hz for each pulse amplitude.

Statistical analyses

We tested the normality of collected data in all experiments using QQ plots. Since not all the datasets were normally distributed, hypothesis testing between two groups was performed using the Mann–Whitney U test. Cumulative distribution functions (CDFs) were measured for individual samples and reshape to equal sample size (n = 500), and the empirical CDF (eCDF) was calculated by averaging these CDFs. The Kolmogorov-Smirnov test was employed to compare eCDFs between groups. Two-way ANOVA was performed for comparing parameters affected by two factors. Values are presented as median (center line), with the 25th (lower bound) and 75th percentiles (upper bound) represented by the box, and whiskers indicating the range in box plots. Statistical significance was considered at $P < 0.05$. Statistical calculations were performed using SciPy (Python). Specific statistical analyses are detailed in the respective figure legends or results section for each dataset.

Figures

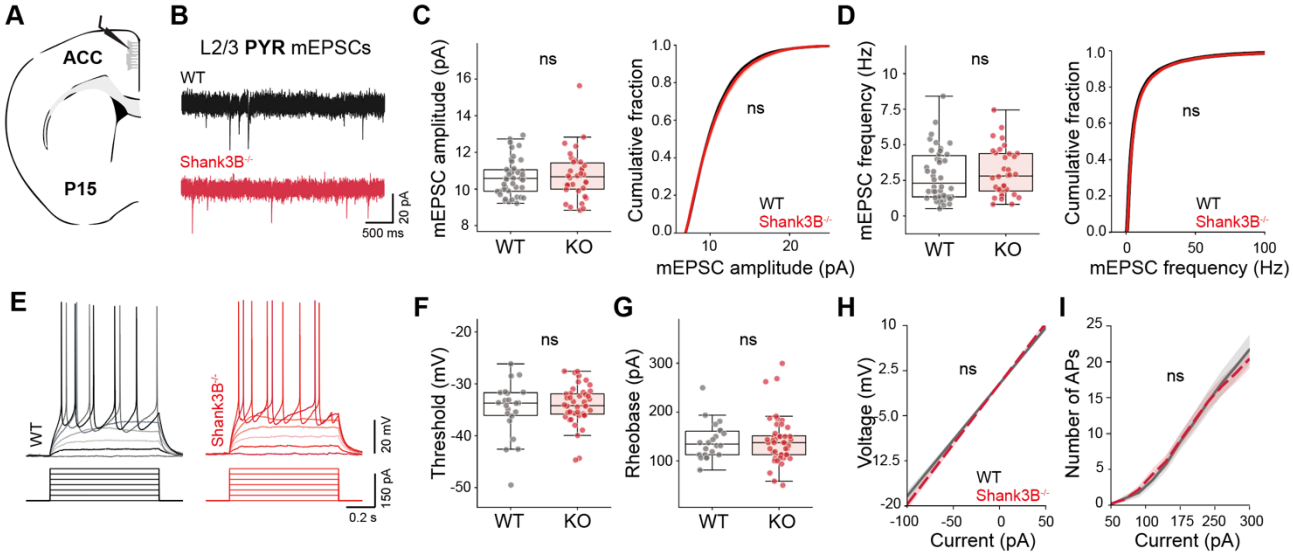

Figure 1. Normal glutamatergic synaptic function and excitability of ACC L2/3 PYR in P15 Shank3B$^{-/-}$ mice. (A) Schematic representing coronal brain section and whole-cell recordings of L2/3 PYR in ACC of P15 mice. **(B)** Representative AMPAR mEPSCs in L2/3 ACC PYR of WT (black) and Shank3B$^{-/-}$ (red) mice. **(C)** Average (left) and cumulative distribution (right) of mEPSC amplitudes and **(D)** frequency per neuron. **(E)** Representative current-clamp recording depicting action potential firing in response to current injection in L2/3 ACC PYR of WT (black) and Shank3B$^{-/-}$ (red) mice. **(F)** Average AP threshold potential and **(G)** rheobase current. **(H)** Voltage-current (I-V) relationship of L2/3 ACC PYR. **(I)** Action potential firing-current (I-F) relationship of L2/3 ACC PYR. For mEPSC recording, n=42,35 neurons from n=4,3 WT and Shank3B$^{-/-}$ mice. For current-clamp recordings, n=25,44 neurons from n=4,5 WT and Shank3B$^{-/-}$ mice. Box plots show median and quartile values. eCDFs represent average of CDF from mEPSCs of each recorded neuron. Box plots *P<0.05 with MW test. eCDFs *P<0.05 with KS test. Regression plots *P<0.05 with two-way ANOVA.

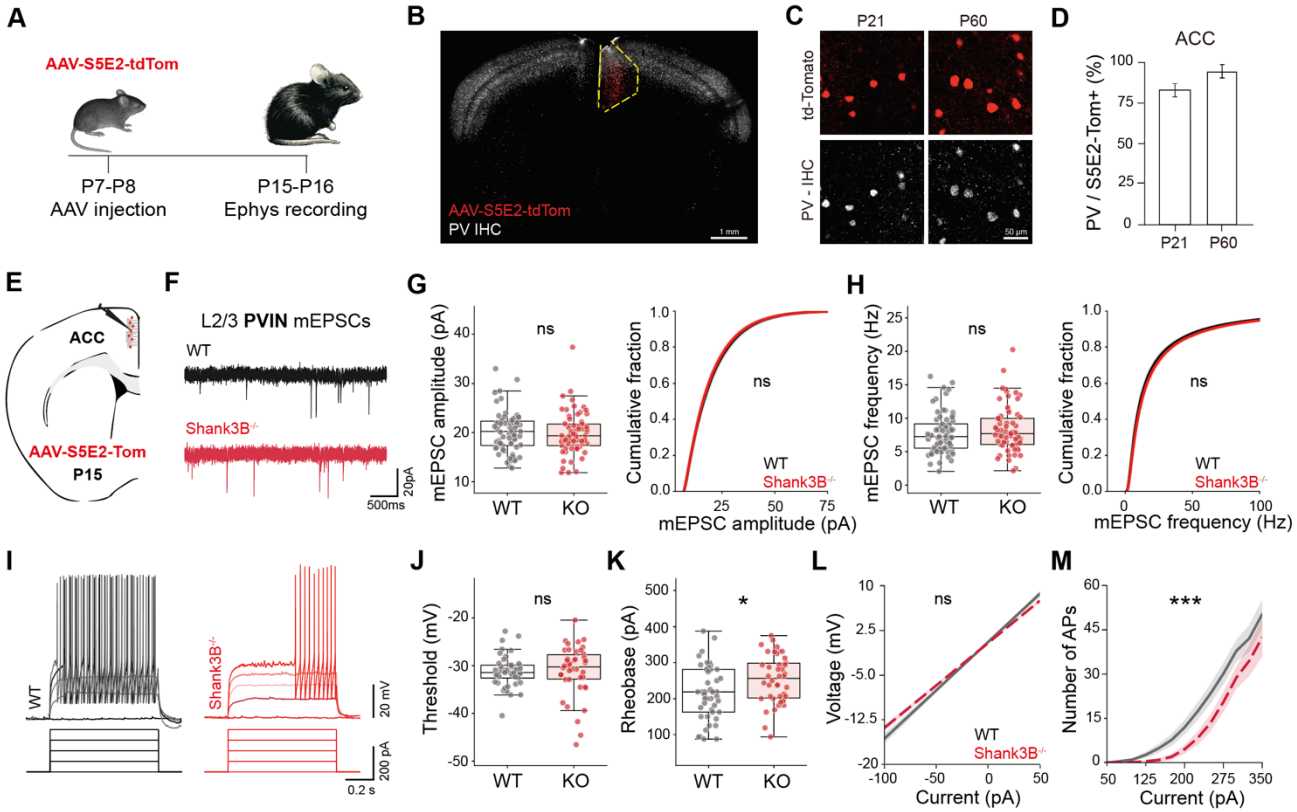

Figure 2. Reduced excitability but normal glutamatergic synaptic inputs of ACC L2/3 S5E2-positive interneurons in P15 Shank3B$^{-/-}$ mice. (A) Schematic of experimental timeline showing AAV-S5E2-tdTomato injection in WT and Shank3B$^{-/-}$ mice at P7-P8, followed by electrophysiological recordings at P15-P16. **(B)** Representative coronal section showing S5E2-Tom expression and PV immunohistochemical labeling in ACC. **(C)** Confocal images of tdTom-positive and PV-positive cells in the ACC at P21 and P60, showing high degree of colocalization. Scale bars = 50µm. **(D)** Quantification of the percentage of PV-positive neurons expressing AAV-S5E2-tdTomato in the ACC at P21 and P60. **(E)** Schematic representing whole-cell recordings in S5E2^{+} interneurons in L2/3 ACC of P15 mice **(F)** Representative AMPAR mEPSCs in L2/3 ACC S5E2^{+} cells of WT (black) and Shank3B$^{-/-}$ (red) mice. **(G)** Average (left) and cumulative distribution (right) of mEPSC amplitude and **(H)** frequency per neuron. **(I)** Representative traces of action potentials recorded in response to step current injections in L2/3 ACC S5E2^{+} interneurons of WT (black) and Shank3B$^{-/-}$ (red) mice. **(J)** Average AP threshold voltage and **(K)** rheobase current. **(L)** I-V relationship of L2/3 ACC S5E2^{+} cells. **(M)** I-F relationship of L2/3 ACC S5E2^{+} cells. For mEPSC recording, n=69,65 neurons from n=6,6 WT and Shank3B$^{-/-}$ mice. For current-clamp recording, n=46,39 neurons from n=5,4 WT and Shank3B$^{-/-}$ mice. Box plots show median and quartile values. eCDFs represent average of CDF from mEPSCs of each recorded neuron. Box plots *P<0.05 with MW test. eCDFs *P<0.05 with KS test. Regression plots ***P<0.001 with two-way ANOVA.

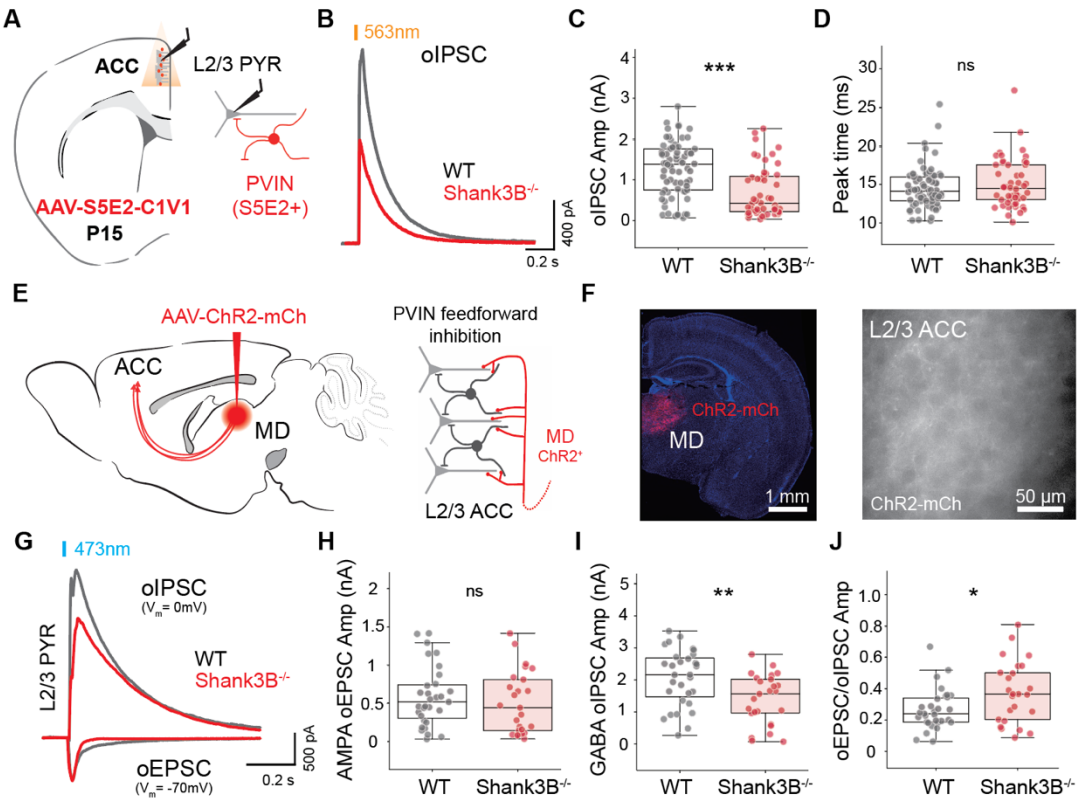

Figure 3. Loss of Shank3 decreases MD-ACC feedforward inhibition onto L2/3 PYR at P15 (A) Schematic representing whole-cell recordings in L2/3 ACC of P15 mice previously injected with AAV-S5E2-C1V1-YFP to express ChR2 in S5E2+ interneurons. **(B)** Representative traces of oIPSCs evoked in L2/3 ACC PYR of WT (black) and Shank3B$^{-/-}$ (red) mice in response to optogenetic stimulation of S5E2^{+} interneurons **(C)** Neuron average oIPSC amplitude and **(D)** peak time. **(E)** Schematic of the viral targeting strategy for optogenetic activation of projections from the mediodorsal thalamus (MD) to the ACC using AAV-ChR2-mCherry. MD fiber stimulation drives PVIN dependent FFI in L2/3 ACC. **(F)** Representative images of ChR2-mCh expression in P15 MD (left) and L2/3 ACC (right). **(G)** Representative oEPSCs (AMPA currents) and oIPSCs (GABA currents) in L2/3 ACC PYR of WT (black) and Shank3B$^{-/-}$ (red) mice. **(H)** Average oEPSC and **(I)** oIPSC peak amplitude per neuron. **(J)** Ratio of oEPSC/oIPSC amplitudes calculated per neuron. For oIPSC recording, n=72,50 neurons from n=5,4 WT and Shank3B$^{-/-}$ mice. For thalamic input recording, n=32,35 neurons from n=4,4 WT and Shank3B$^{-/-}$ mice. Box plots show median and quartile values. Box plots *P<0.05, **P<0.01, ***P<0.001 with MW U test.

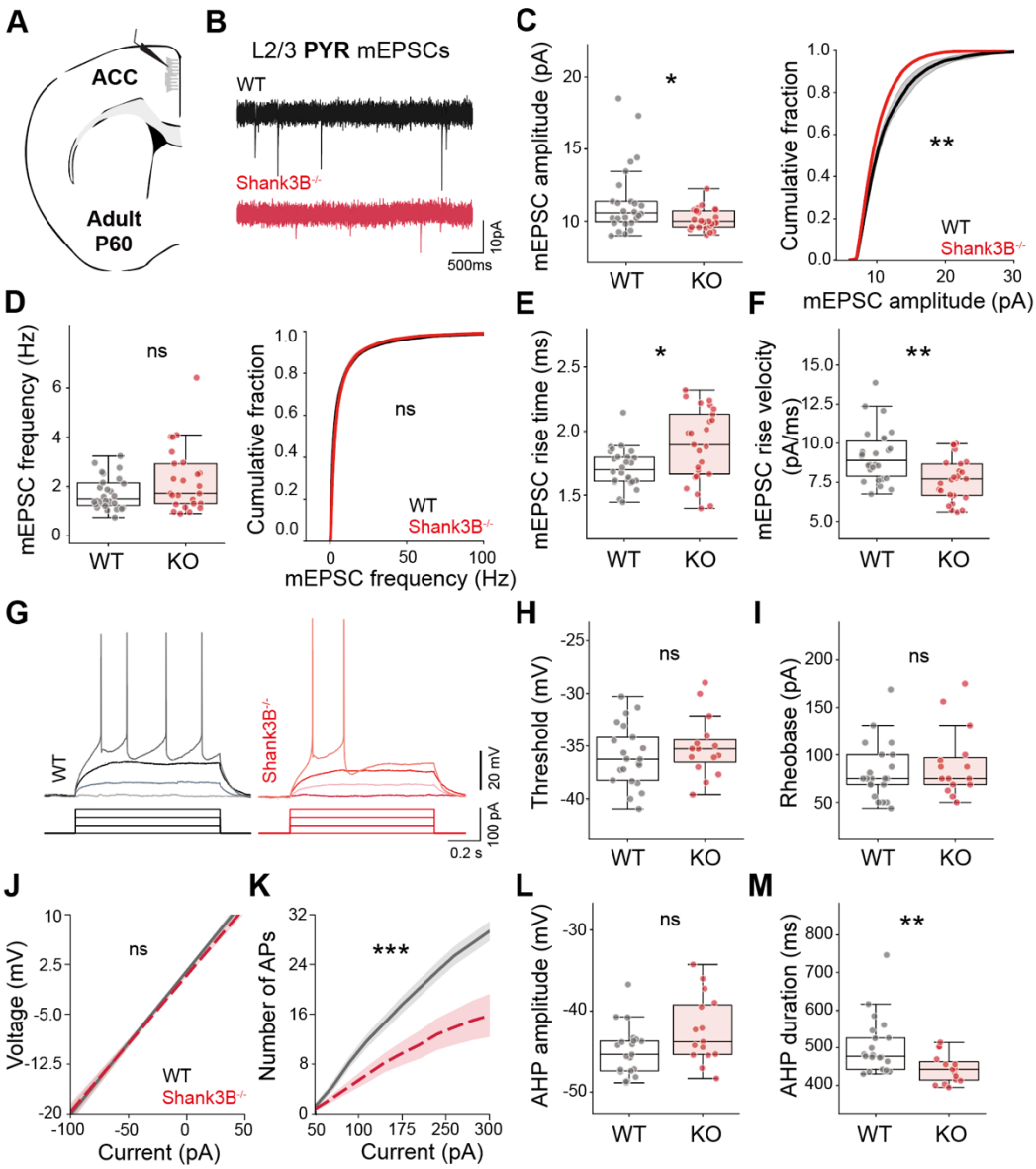

Figure 4. Reduced glutamatergic synaptic strength and hypoexcitability of ACC L2/3 PYR in Adult Shank3B$^{-/-}$ mice. (A) Schematic representing coronal brain section and whole-cell recordings of L2/3 PYR in ACC of P60 mice. **(B)** Representative AMPAR mEPSCs recorded in L2/3 ACC PYR of WT (black) and Shank3B$^{-/-}$ (red) mice. **(C)** Average (left) and cumulative distribution (right) of mEPSC amplitude and **(D)** frequency per neuron. **(E)** Average mEPSC rise time and **(F)** velocity per neuron showing slower mEPSC kinetics in adult L2/3 ACC PYR of Shank3B$^{-/-}$ mice. **(G)** Representative current-clamp recordings in L2/3 ACC PYR of WT (black) and Shank3B$^{-/-}$ (red) mice. **(H)** Average of AP threshold. **(I)** rheobase current per neuron. **(J)** I-V and **(K)** I-F relationship of L2/3 ACC PYR. **(L)** Average afterhyperpolarization current amplitude and **(M)** duration per neuron. For mEPSC recording, n=26,25 neurons from n=3,3 WT and Shank3B$^{-/-}$ mice. For current-clamp recording, n=24,16 neurons from n=3,2 WT and Shank3B$^{-/-}$ mice. Box plots show median and quartile values. eCDFs represent average of CDF from mEPSCs of each recorded neuron. Box plots *P<0.05 with MW test. eCDFs **P<0.01 with KS test. Regression plots ***P<0.001 with two-way ANOVA.

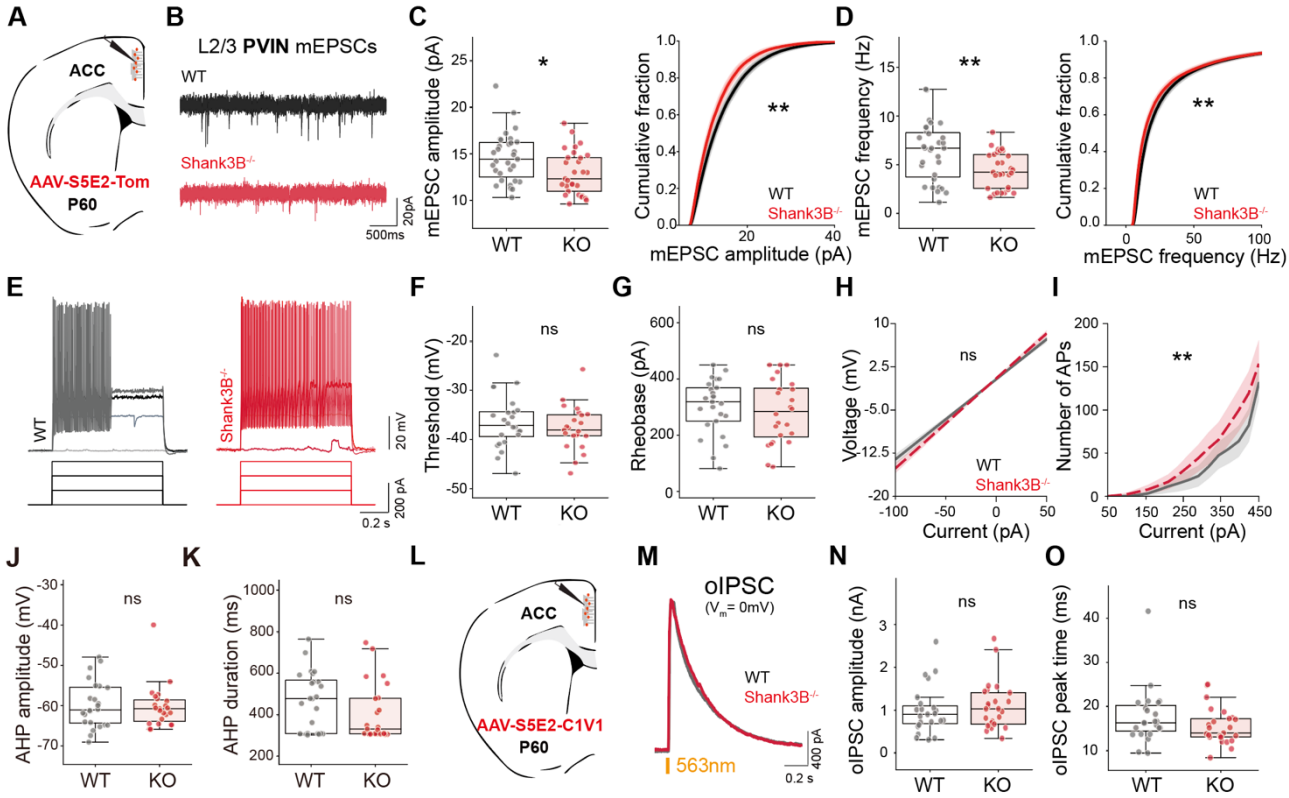

Figure 5. Adult-stage adaptations in synaptic and intrinsic excitability in L2/3 ACC PVIN of adult Shank3B$^{-/-}$ mice. (A) Schematic representing whole-cell recordings in S5E2^{+} interneurons in L2/3 ACC of P60 mice **(B)** Representative AMPAR mEPSCs in L2/3 ACC S5E2^{+} cells of WT (black) and Shank3B$^{-/-}$ (red) mice. **(C)** Average (left) and cumulative distribution (right) of mEPSC amplitude and **(D)** frequency per neuron. **(E)** Representative traces of current-clamp recordings in L2/3 ACC S5E2^{+} interneurons of WT (black) and Shank3B$^{-/-}$ (red) mice. **(F)** Average of AP threshold potential and **(G)** rheobase current. **(H)** I-V and **(I)** I-F relationship of L2/3 ACC S5E2^{+} cells. **(J)** Average afterhyperpolarization current amplitude and **(K)** duration per neuron. **(K)** Schematic representing coronal brain section and whole-cell recordings in L2/3 ACC on adult mice previously injected with AAV-S5E2-C1V1-YFP for optogenetic stimulation of S5E2^{+} interneurons. **(M)** Representative S5E2-dependent oIPSCs in L2/3 ACC PYR of adult WT (black) and Shank3B$^{-/-}$ (WT) mice. **(N)** Average oIPSC amplitude and **(O)** peak time. For PYR mEPSC recording, n=26,25 neurons from n=3,3 WT and Shank3B$^{-/-}$ mice. For PYR current-clamp recording, n=24,16 neurons from n=3,2 WT and Shank3B$^{-/-}$ mice. For E2+ mEPSC recording, n=31,31 neurons from n=5,4 WT and Shank3B$^{-/-}$ mice. For E2^{+} current-clamp recording, n=25,24 neurons from n=3,3 WT and Shank3B$^{-/-}$ mice. For oIPSC recording, n=23,25 neurons from n=4,4 WT and Shank3B$^{-/-}$ mice. Box plots show median and quartile values. eCDFs represent average of CDF from mEPSCs of each recorded neuron. Box plots *P<0.05 with MW test. eCDFs *P<0.05 with KS test. Regression plots **P<0.01 with two-way ANOVA.

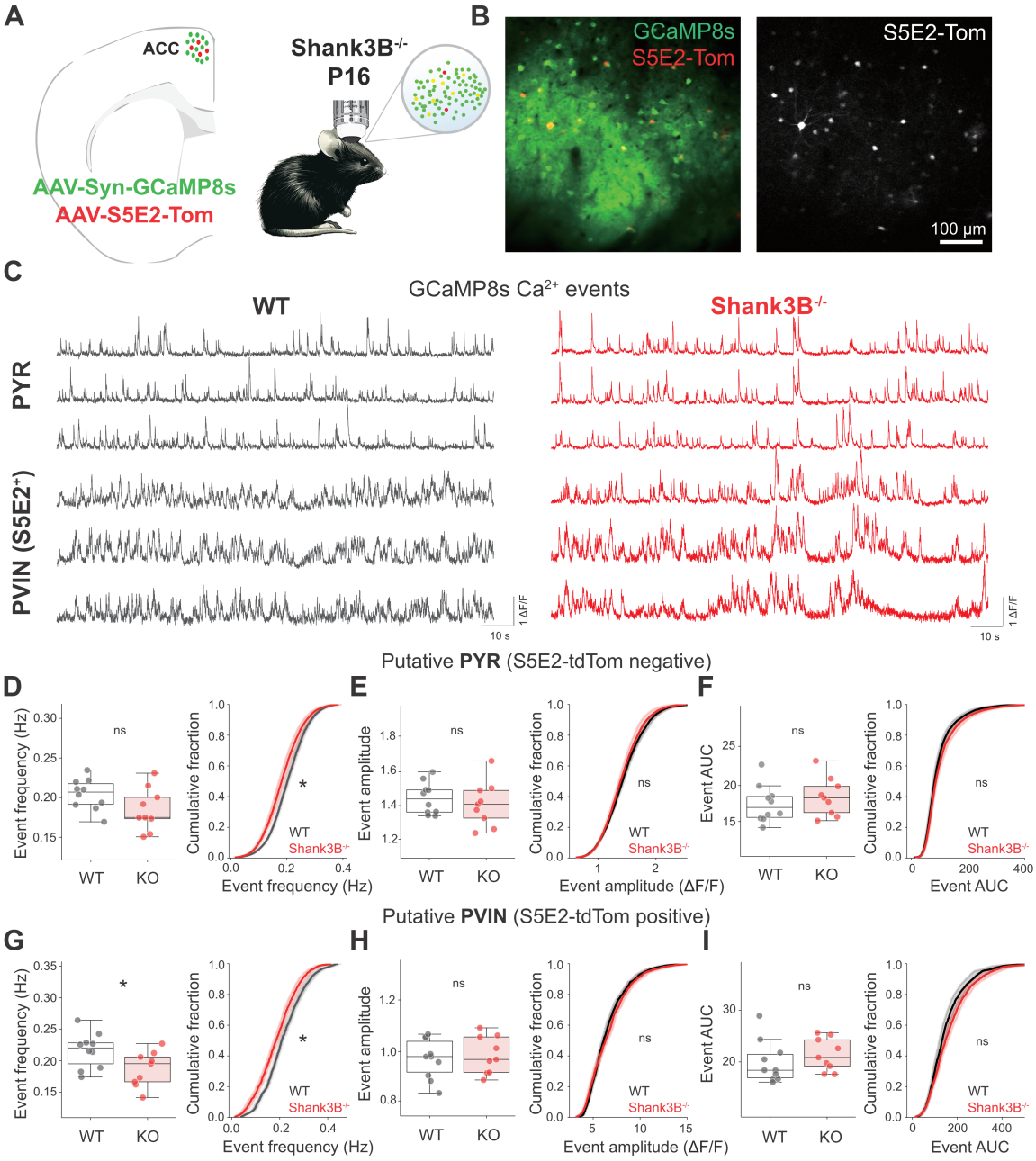

Figure 6. Reduced frequency of Ca^{2+} transients in ACC PYR and S5E2+ interneurons of P15-P17 Shank3B$^{-/-}$ mice.

(A) Schematic diagram of in vivo calcium imaging in dorsal ACC of mouse co-injected with AAV9-GCaMP8s and AAV5-S5E2-tdTom in dACC. Imaging was performed in a 2-photon microscope through a cranial window. **(B)** Fluorescent images showing co-expression of GCaMP8s (green) and S5E2-tdTomato (red) in the dACC. Right panel shows S5E2-tdTomato positive interneurons. Scale bar = 100 µm. **(C)** Representative traces of GCaMP8s calcium events from putative pyramidal (S5E2-tdTom negative) neurons and PVIN (S5E2-Tom positive) neurons in WT (black) and KO (red) mice. **(D)** Average (left) and cumulative distribution (right) of GCaMP8s event frequency, **(E)** amplitude and **(F)** duration (area under the curve) of putative PYR. **(G)** Average (left) and cumulative distribution (right) of GCaMP8s event frequency **(H)** amplitude and **(I)** duration (area under the curve) of putative PVIN. n=10,9 WT and Shank3B$^{-/-}$ mice. Box plots show median and quartile values. Box plots *P<0.05 with MW test. eCDFs *P<0.05 with KS test.

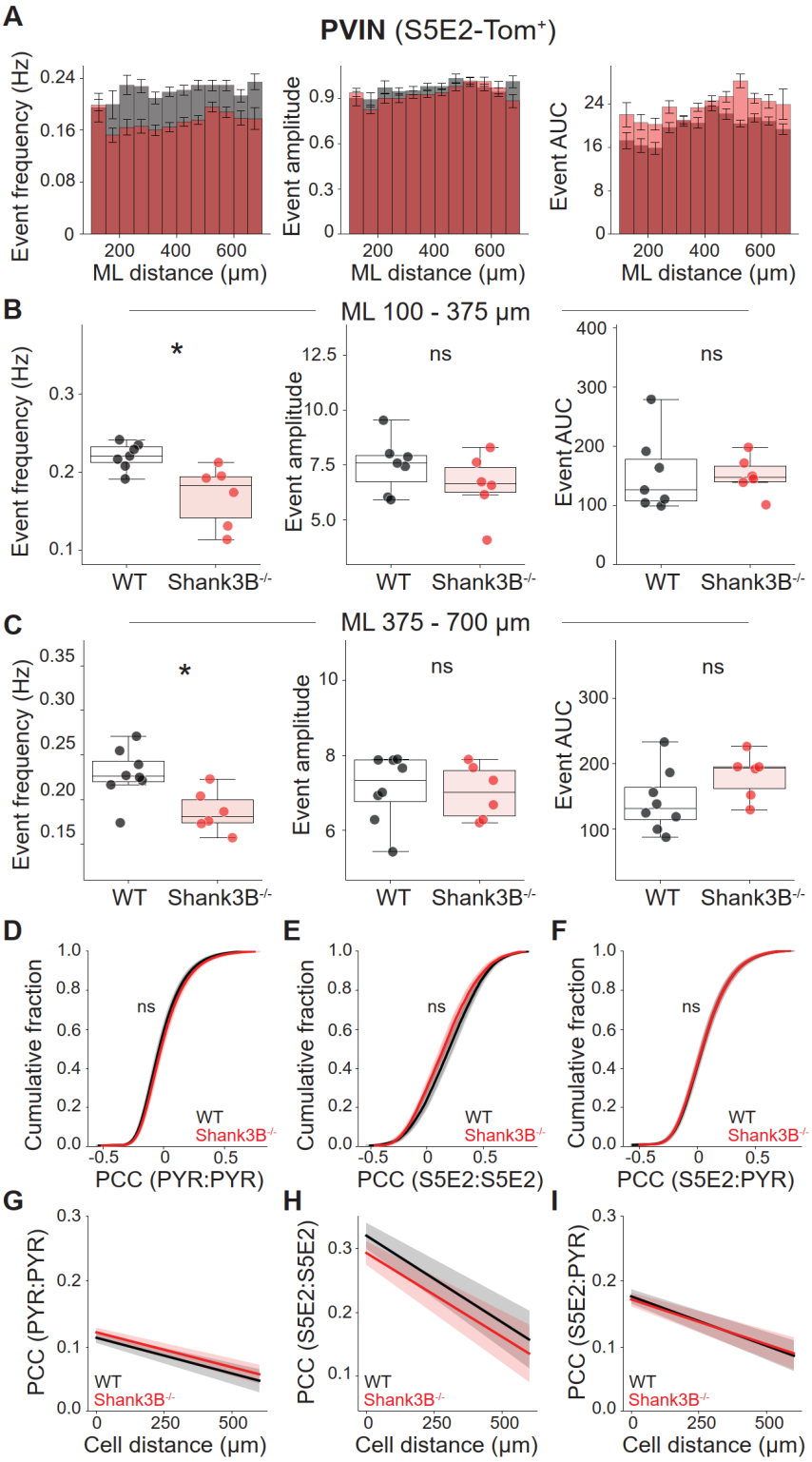

Figure 7. No difference in layer and activity correlation in ACC of P15-P17 Shank3B$^{-/-}$ mice.

(A) Bar plots of event frequency, amplitude, and AUC of putative PVIN across mediolateral (ML) distance for WT (gray) and KO (red) mice. Cells are grouped in every 50 µm ML distance. **(B)** Average of GCaMP8s event frequency, amplitude, and AUC of putative PVIN in superficial layer (100<ML≤375 µm). **(C)** Average of GCaMP8s event frequency, amplitude, and AUC of putative PVIN in deep layer (ML>375 µm). **(D-F)** Cumulative distribution of Pearson correlation coefficient (PCC) of activity between different neuronal populations. **(G-I)** Linear regressions of PCC against to cell distance. n=8,6 WT and Shank3B$^{-/-}$ mice. Box plots show median and quartile values. Box plots *P<0.05 with MW test. eCDFs *P<0.05 with Kolmogorov-Smirnov test.

Supplemental Figures

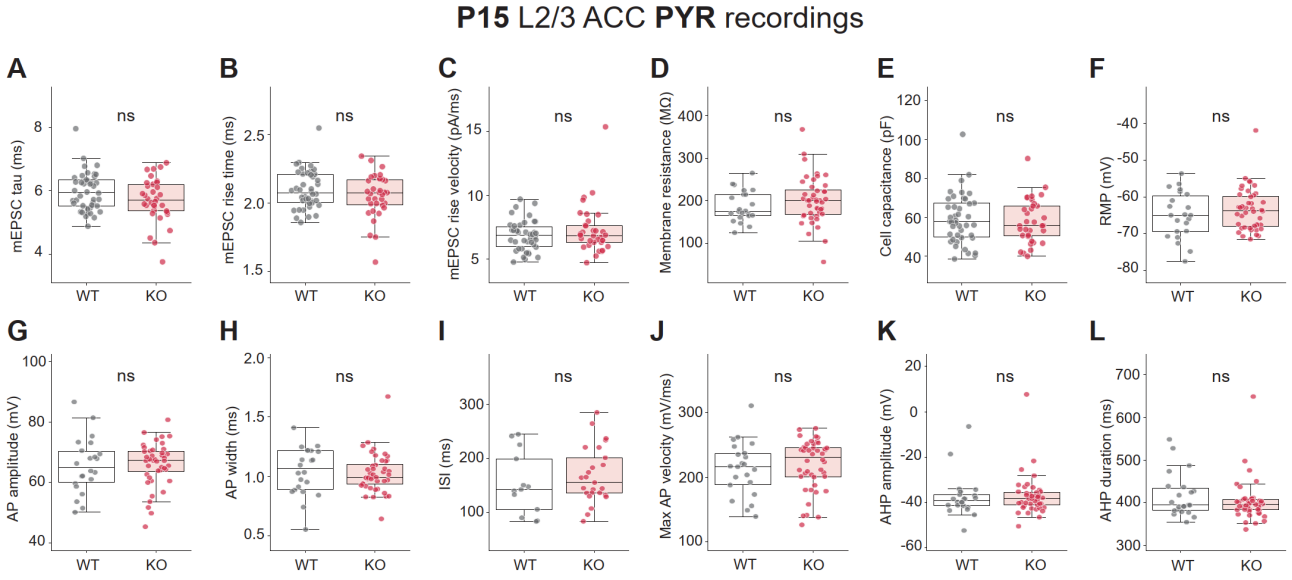

Supplementary figure 1. mEPSC and action potential properties of L2/3 PYR in ACC of P15 Shank3B$^{-/-}$ mice. (A) Average mEPSC tau of PYR, WT 6.0±0.6ms; KO 5.7±0.7ms, MW test p=0.17. **(B)** Average mEPSC rise time of PYR, WT 2.1±0.1ms; KO 2.1±0.2ms, MW test p=0.37. **(C)** Average mEPSC rise velocity of PYR, WT 6.8±1.2pA/ms; KO 7.3±1.9pA/ms, MW test p=0.6. **(D)** Average membrane resistance of PYR, WT 190.4±39.6MΩ; KO 199.3±54.7MΩ, MW test p=0.28. **(E)** Average cell capacitance of PYR, WT 59.1±12.9pF; KO 57.9±11.4pF, MW test p=0.65. **(F)** Average resting membrane potential of PYR, WT -65.2±6.6mV; KO -63.6±5.7mV, MW test p=0.47. **(G)** Average AP amplitude of PYR, WT 65.6±9.0mV; KO 66.5±6.5mV, MW test p=0.58. **(H)** Average AP width of PYR, WT 1.1±0.2ms; KO 1.0±0.2ms, MW test p=0.48. **(I)** Average inter-spike interval of PYR, WT 159.6±52.5ms; KO 168.6±51.8ms, MW test p=0.44. **(J)** Average maximum AP velocity of PYR, WT 210.3±38.4mV/ms; KO 221.2±37.3mV/ms, MW test p=0.38. **(K)** Average afterhyperpolarization amplitude of PYR, WT -36.2±9.3mV; KO -37.0±8.8mV, MW test p=0.57. **(L)** Average afterhyperpolarization duration of PYR, WT 412.6±45.2ms; KO 404.6±47.5ms, MW test p=0.51. For mEPSC recording, n=26,25 neurons from n=3,3 WT and Shank3B$^{-/-}$ mice. For current-clamp recording, n=24,16 neurons from n=3,2 WT and Shank3B$^{-/-}$ mice. Box plots show median and quartile values. Box plots *P<0.05 with MW test.

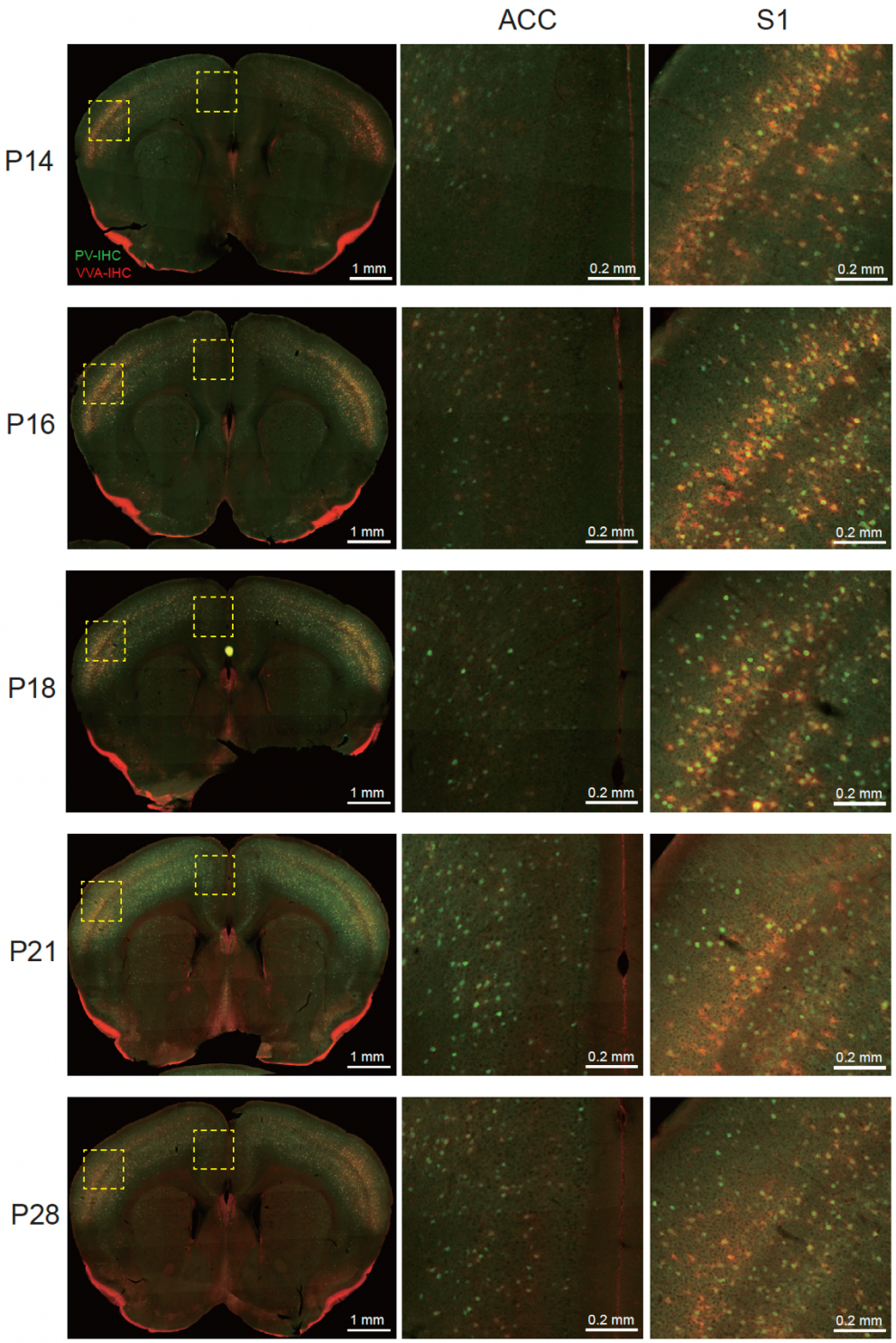

Supplementary figure 2. Developmental expression of Parvalbumin and VVA in the anterior cingulate cortex (ACC) and somatosensory cortex (S1). Representative coronal brain sections of WT mice at postnatal days P14, P16, P18, P21, and P28. Immunohistochemistry (IHC) for Parvalbumin (PV, green) and the perineuronal net marker Vicia Villosa Agglutinin (VVA, red) shows the distribution and density of PV-INs and VVA nets in the ACC (middle panels) and S1 (right panels). The yellow dashed boxes in the whole brain images (left panels) indicate the regions of the ACC and S1 that are magnified in the middle and right columns, respectively. Note that expression of PV in ACC is delayed in comparison with S1, only reaching full uniform expression by P21. Scale bars: 1 mm for whole brain sections, 0.2 mm for magnified regions.

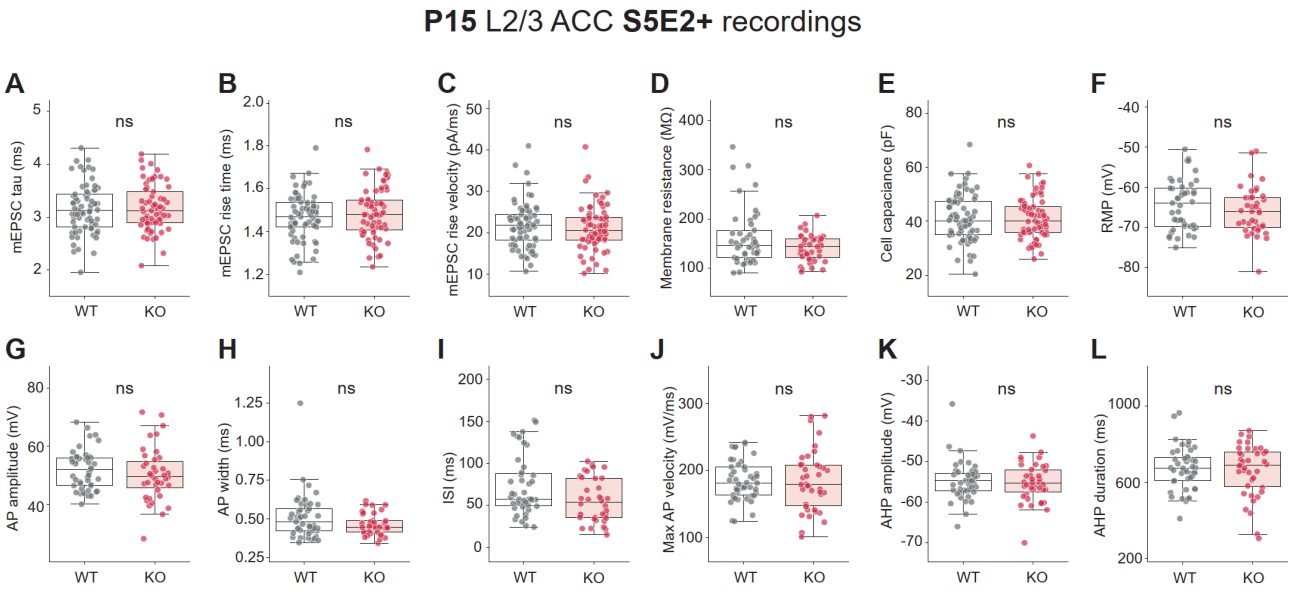

Supplementary figure 3. mEPSC and action potential properties of L2/3 S5E2-Tom positive interneurons in ACC of P15 Shank3B$^{-/-}$ mice. (A) Average mEPSC tau of S5E2-Tom+ interneurons, WT 3.2±0.5ms; KO 3.2±0.4ms, MW test p=0.92. **(B)** Average mEPSC rise time of S5E2-Tom+ interneurons, WT 1.5±0.1ms; KO 1.5±0.1ms, MW test p=0.47. **(C)** Average mEPSC rise velocity of S5E2-Tom+ interneurons, WT 21.7±5.5pA/ms; KO 21.1±5.5pA/ms, MW test p=0.52. **(D)** Average membrane resistance of S5E2-Tom+ interneurons, WT 162.1±58.3 MΩ; KO 140.2±28 MΩ, MW test p=0.25. **(E)** Average cell capacitance of E2-Tom+ interneurons, WT 41.1±8.8pF; KO 41.2±7.6pF, MW test p=0.94. **(F)** Average resting membrane potential of S5E2-Tom+ interneurons, WT -64.3±6.2 mV; KO -66.0±5.9mV, MW test p=0.28. **(G)** Average AP amplitude of S5E2-Tom+ interneurons, WT 52.0±6.8 mV; KO 50.7±9.3 mV, MW test p=0.33. **(H)** Average AP width of S5E2-Tom+ interneurons, WT 0.5±0.2ms; KO 0.5±0.1ms, MW test p=0.21. **(I)** Average inter-spike interval of S5E2-Tom+ interneurons, WT 72.7±35.4ms; KO 55.0±25.5ms, MW test p=0.21. **(J)** Average maximum AP velocity of S5E2-Tom+ interneurons, WT 184.7±29.7mV/ms; KO 185.6±45.8mV/ms, MW test p=0.86. **(K)** Average afterhyperpolarization amplitude of S5E2-Tom+ interneurons, WT -54.7±4.7mV; KO -55.7±4.3mV, MW test p=0.72. **(L)** Average afterhyperpolarization duration of E2-Tom+ interneurons, WT 672.2±112.7ms; KO 653.4±133.7ms, MW test p=0.51. For mEPSC recording, n=69,65 neurons from n=6,6 WT and Shank3B$^{-/-}$ mice. For current-clamp recording, n=46,39 neurons from n=5,4 WT and Shank3B$^{-/-}$ mice. Box plots show median and quartile plots. Box plots *P<0.05 with MW test.

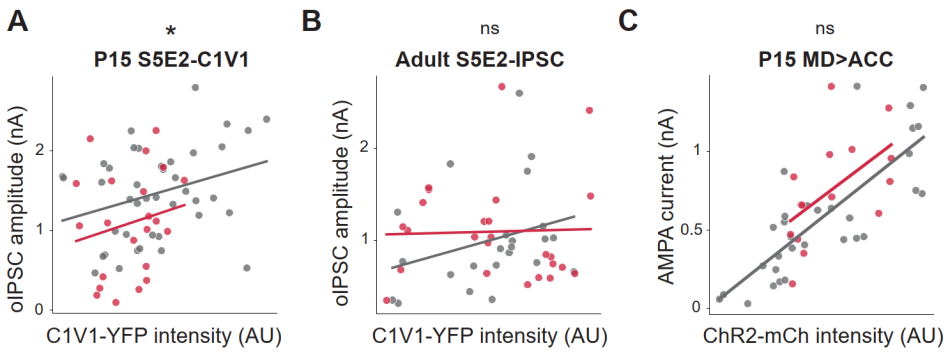

Supplementary figure 4. Relationship between opsin expressing fiber fluorescence intensity and optogenetically evoked currents. **(A)** Relationship between YFP intensity (C1V1-YFP expressing S5E2+ interneurons) and oIPSC amplitude evoked on L2/3 ACC PYR in P15 (two-way ANOVA p=0.036 in genotype) and **(B)** adult WT (black) and Shank3B$^{-/-}$ (red) mice (two-way ANOVA p = 0.33 in genotype). **(C)** Relationship between mCherry intensity (ChR2-mCh expressing fibers from MD) and AMPA currents evoked on L2/3 ACC PYR in P15, two-way ANOVA p=0.12 in genotype. For P15 oIPSC recording, n=42,22 neurons from n=5,3 WT and Shank3B$^{-/-}$ mice. For P15 thalamic input recording, n=31,15 neurons from n=4,2 WT and Shank3B$^{-/-}$ mice. For adult oIPSC recording, n=23,25 neurons from n=4,4 WT and Shank3B$^{-/-}$ mice. Scatter plots *P<0.05 with two-way ANOVA.

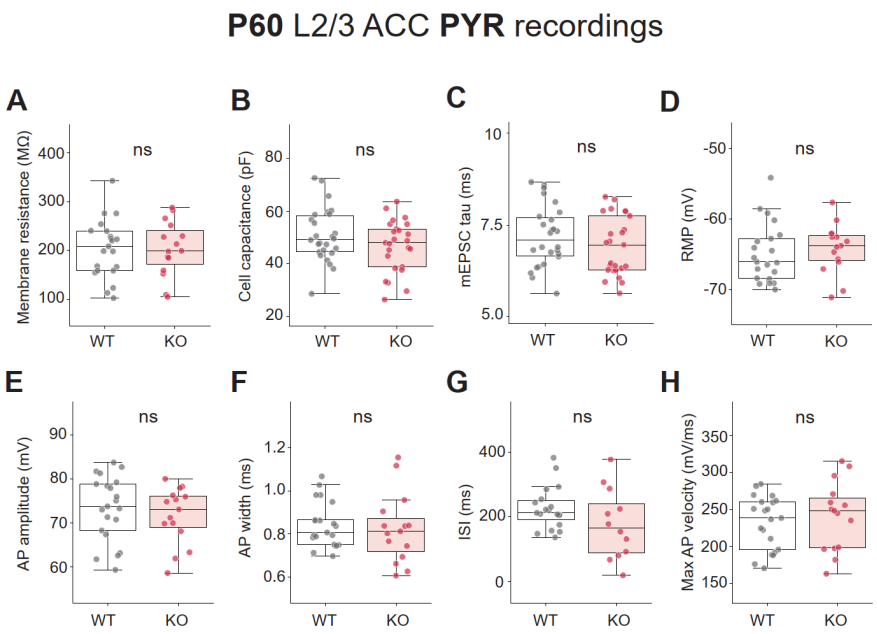

Supplementary figure 5. mEPSC and action potential properties of L2/3 PYR in ACC of P60 Shank3B$^{-/-}$ mice. **(A)** Average membrane resistance of PYR. **(B)** Average cell capacitance of PYR, WT 51.0±10.2pF; KO 46.8±9.8pF, MW test p=0.3. **(C)** Average mEPSC tau of PYR, WT 7.2±0.8 ms; KO 6.9±0.8 ms, MW test p=0.28. **(D)** Average resting membrane potential of PYR, WT -64.9±6.2 mV; KO -64.2±3.5 mV, MW test p=0.35. **(E)** Average AP amplitude PYR, WT 73.3±7.3 mV; KO 71.7±6.4 mV, MW test p=0.42. **(F)** Average AP width of PYR, WT 0.8±0.1 ms; KO 0.8±0.2 ms, MW test p=0.56. **(G)** Average inter-spike interval of PYR, WT 225.8±65.5 ms; KO 177.2±107.8 ms, MW test p=0.17. **(H)** Average maximum AP velocity of PYR, WT 232.4±35.8 mV/ms; KO 241.5±46.1 mV/ms, MW test p=0.63. For mEPSC recording, n=26,25 neurons from n=3,3 WT and Shank3B$^{-/-}$ mice. For current-clamp recording, n=24,16 neurons from n=3,2 WT and Shank3B$^{-/-}$ mice. Box plots show median and quartile values. Box plots *P<0.05, **P<0.01 with MW test.

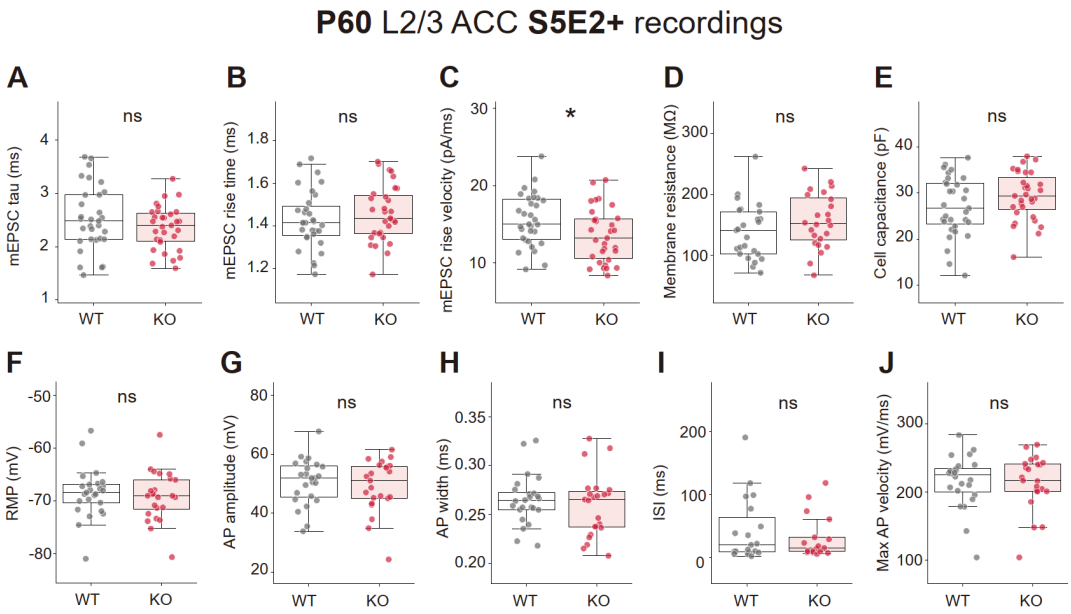

Supplementary figure 6. mEPSC and action potential properties of L2/3 S5E2-Tom positive interneurons in ACC of adult Shank3B$^{-/-}$ mice. (A) Average±SD mEPSC tau of S5E2-Tom+ interneurons, WT 2.5±0.6 ms; KO 2.4±0.4 ms, MW test p=0.4. **(B)** Average mEPSC rise time of S5E2-Tom+ interneurons, WT 1.4±0.1 ms; KO 1.5±0.1 ms, MW test p=0.33. **(C)** Average mEPSC rise velocity of S5E2-Tom+ interneurons, WT 15.6±3.3 pA/ms; KO 13.4±3.5 pA/ms, MW test p=0.02. **(D)** Average membrane resistance of S5E2-Tom+ interneurons, WT 140.8±45.9MΩ; KO 153.3±44.7MΩ, MW test p=0.16. **(E)** Average cell capacitance of E2-Tom+ interneurons, WT 27.1±6.5 pF; KO 28.9±5.0 pF, MW test p=0.32. **(F)** Average resting membrane potential of S5E2-Tom+ interneurons, WT -68.9±4.1 mV; KO -69.3±4.8 mV, MW test p=0.58. **(G)** Average AP amplitude of S5E2-Tom+ interneurons, WT 51.0±7.4 mV; KO 51.1±6.5 mV, MW test p=0.81. **(H)** Average AP width of S5E2-Tom+ interneurons, WT 0.3±0.0 ms; KO 0.3±0.0 ms, MW test p=0.6. **(I)** Average inter-spike interval of S5E2-Tom+ interneurons, WT 45.7±51.5 ms; KO 35.3±35.4 ms, MW test p=0.79. **(J)** Average maximum AP velocity of S5E2-Tom+ interneurons, WT 219.5±31.4 mV/ms; KO 222.5±28.6 mV/ms, MW test p = 0.92. For mEPSC recording, n=31,31 neurons from n=5,4 WT and Shank3B$^{-/-}$ mice. For current-clamp recording, n=25,24 neurons from n=3,3 WT and Shank3B$^{-/-}$ mice. Box plots show median and quartile values. Box plots *P<0.05 with MW test.

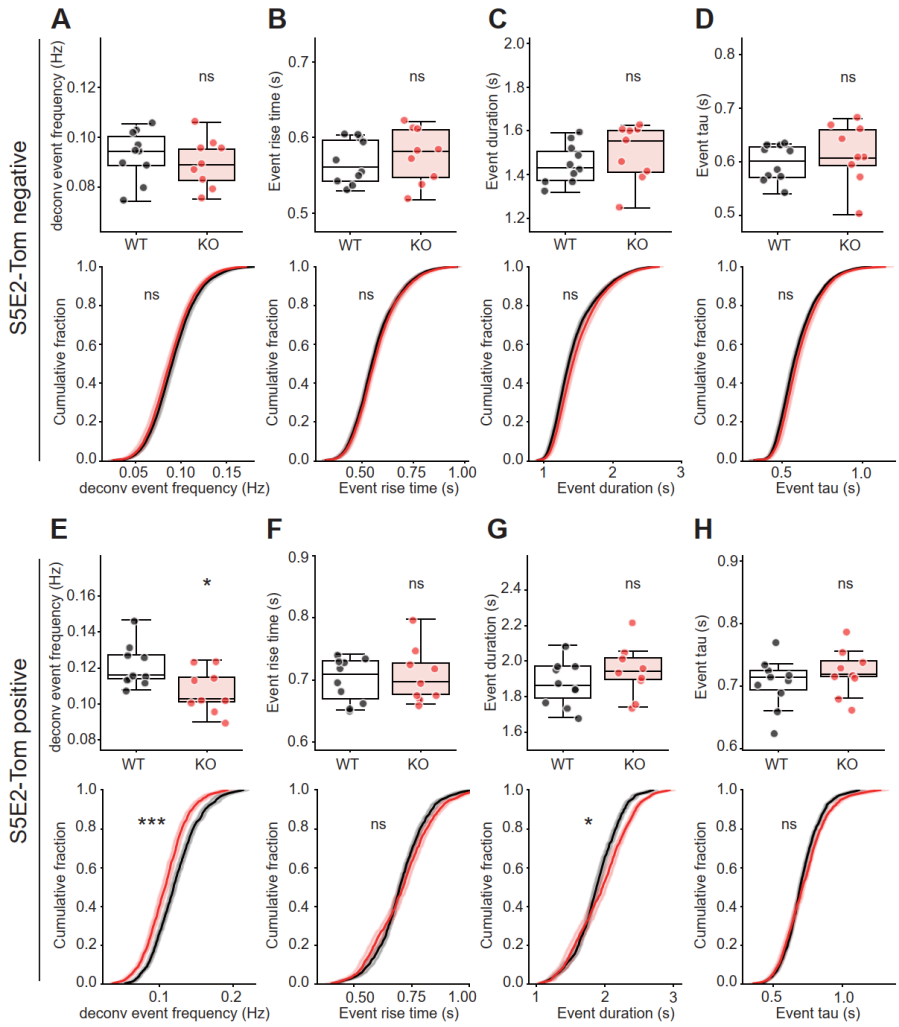

Supplementary figure 7. Reduced deconvolved event frequency of S5E2-Tom positive cells in dorsal ACC of P16 Shank3B$^{-/-}$ mice was consistent to decrease of z-scored event frequency. (A) Average±SD (upper) and cumulative distribution (lower) of GCaMP8s deconvolved event frequency from E2-Tom- cells, WT 0.09±0.01Hz; KO 0.09±0.01Hz, MW test p=0.60, KS test p=0.89. **(B)** Average±SD (upper) and cumulative distribution (lower) of GCaMP8s event rise time from E2-Tom- cells, WT 0.57±0.03s; KO 0.58±0.04s, MW test p=0.54, KS test p=0.87. **(C)** Average ±SD (upper) and cumulative distribution (lower) of GCaMP8s event duration from E2-Tom- cells, WT 1.45±0.09s; KO 1.50±0.13s, MW test p=0.21, KS test p=0.29. **(D)** Average ±SD (upper) and cumulative distribution (lower) of GCaMP8s event tau from E2-Tom- cells, WT 0.6±0.03s; KO 0.61±0.06s, MW test p=0.35, KS test p=0.54. **(E)** Average ±SD (upper) and cumulative distribution (lower) of GCaMP8s deconvolved event frequency from E2-Tom+ cells, WT 0.12±0.01Hz; KO 0.11±0.01Hz, MW test p=0.03, KS test p=8e-4. **(F)** Average±SD (upper) and cumulative distribution (lower) of GCaMP8s event rise time from E2-Tom+ cells, WT 0.70±0.04s; KO 0.71±0.04s, MW test p=0.97, KS test p=0.47. **(G)** Average ±SD (upper) and cumulative distribution (lower) of GCaMP8s event duration from E2-Tom+ cells, WT 1.88±0.13s; KO 1.95±0.15s, MW test p=0.35, KS test p=0.03. **(H)** Average ±SD (upper) and cumulative distribution (lower) of GCaMP8s event tau from E2-Tom+ cells, WT 0.71±0.04s; KO 0.72±0.04s, MW test p=0.35, KS test p=0.29. n=10,9 WT and Shank3B$^{-/-}$ mice. Box plots show median and quartile values. Box plots *P<0.05 with MW test. eCDFs *P<0.05, ***P<0.001 with KS test.

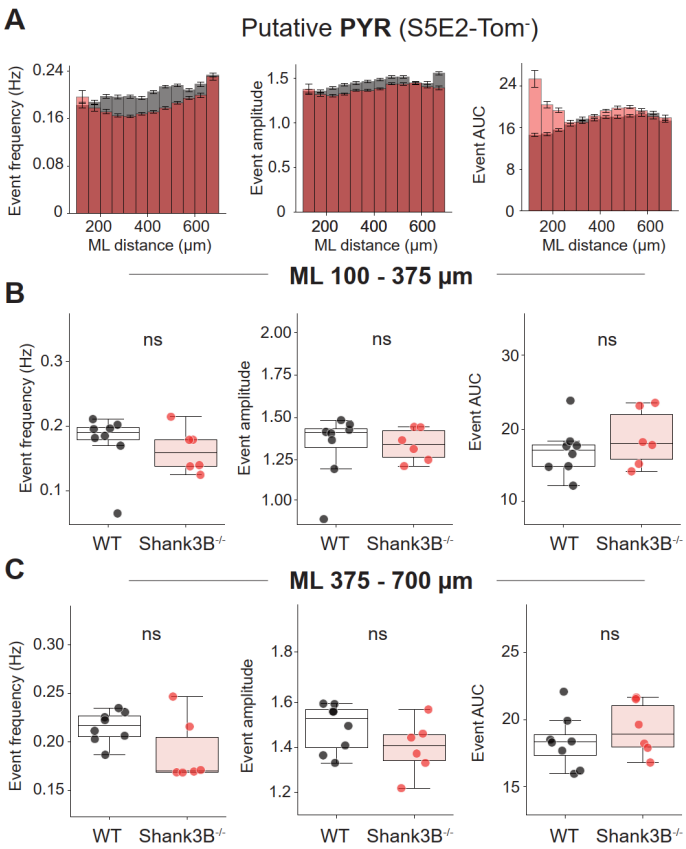

Supplementary figure 8. Laminar and mediolateral distance-dependent analysis of calcium event properties in putative pyramidal (S5E2-) in Shank3B$^{-/-}$ mice. (A) Bar plots showing the mean ± SEM event frequency, amplitude, and area under the curve (AUC) as a function of mediolateral (ML) distance in putative pyramidal (S5E2-negative) neurons of WT (gray) and KO (red) mice. No significant ML-dependent differences are observed. **(B)** Box plots showing the event frequency, amplitude, and AUC of calcium events in putative pyramidal neurons in Layer 2/3 ACC of WT and KO mice, average±SD superficial PYR event frequency, WT 0.18±0.05 Hz; KO 0.16±0.03 Hz, MW test p=0.28. Average ±SD superficial PYR event amplitude, WT 1.3±0.2; KO 1.3±0.1, MW test p=0.66. Average±SD superficial PYR event AUC, WT 17.3±3.5; KO 19.1±4.0, MW test p=0.49. **(C)** Box plots showing the event frequency, amplitude, and AUC of calcium events in putative pyramidal neurons in Layer 5 ACC of WT and KO mice. n=8,6 WT and Shank3B$^{-/-}$ mice, average±SD deep PYR event frequency, WT 0.22±0.02 Hz; KO 0.19±0.03 Hz, MW test p = 0.14. Average ±SD deep PYR event amplitude, WT 1.5±0.1; KO 1.4±0.1, MW test p=0.28. Average±SD deep PYR event AUC, WT 18.2±2.1; KO 19.2±2.1, MW test p=0.66. Box plots show median and quartile values. Box plots *P<0.05 with MW test.

Bibliography

1. Watts, T. J. The pathogenesis of autism. *Clin Med Pathol* (2008) doi:PMC3160002.
2. Amaral, D. G., Schumann, C. M. & Nordahl, C. W. Neuroanatomy of autism. *Trends Neurosci* **31**, 137–145 (2008).
3. Gilbert, S. J., Bird, G., Brindley, R., Frith, C. D. & Burgess, P. W. Atypical recruitment of medial prefrontal cortex in autism spectrum disorders: an fMRI study of two executive function tasks. *Neuropsychologia* **46**, 2281–91 (2008).
4. Assaf, M. *et al.* Abnormal functional connectivity of default mode sub-networks in autism spectrum disorder patients. *Neuroimage* **53**, 247–256 (2010).
5. Goldberg, M. C. *et al.* Children with high functioning autism show increased prefrontal and temporal cortex activity during error monitoring. *Dev Cogn Neurosci* **1**, 47–56 (2011).
6. Sumiya, M. *et al.* Attenuated activation of the anterior rostral medial prefrontal cortex on self-relevant social reward processing in individuals with autism spectrum disorder. *Neuroimage Clin* **26**, 102249 (2020).
7. Zhao, H.-C. *et al.* Alterations of Prefrontal-Posterior Information Processing Patterns in Autism Spectrum Disorders. *Front Neurosci* **15**, 768219 (2021).
8. Lewine, J. D. *et al.* Magnetoencephalographic patterns of epileptiform activity in children with regressive autism spectrum disorders. *Pediatrics* **104**, 405–418 (1999).
9. Khan, O. I. *et al.* Prospective longitudinal overnight video-EEG evaluation in Phelan–McDermid Syndrome. *Epilepsy and Behavior* (2018) doi:10.1016/j.yebeh.2017.11.034.
10. Tuchman, R. & Rapin, I. Epilepsy in autism. *Lancet Neurol* **1**, 352–358 (2002).
11. Amiet, C. *et al.* Epilepsy in Autism is Associated with Intellectual Disability and Gender: Evidence from a Meta-Analysis. *Biol Psychiatry* **64**, 577–582 (2008).
12. Brumback, A. C. *et al.* Identifying specific prefrontal neurons that contribute to autism-associated abnormalities in physiology and social behavior. *Mol Psychiatry* **23**, 2078–2089 (2018).
13. Frost, N. A., Haggart, A. & Sohal, V. S. *Dynamic Patterns of Correlated Activity in the Prefrontal Cortex Encode Information about Social Behavior*. *PLoS Biology* vol. 19 (2021).
14. Qiu, S., Anderson, C. T., Levitt, P. & Shepherd, G. M. G. Circuit-Specific Intracortical Hyperconnectivity in Mice with Deletion of the Autism-Associated *Met* Receptor Tyrosine Kinase. *The Journal of Neuroscience* **31**, 5855–5864 (2011).
15. Kalmbach, B. E., Johnston, D. & Brager, D. H. Cell-Type Specific Channelopathies in the Prefrontal Cortex of the *fmr1-/y* Mouse Model of Fragile X Syndrome. *eNeuro* **2**, ENEURO.0114-15.2015 (2015).
16. Klune, C. B., Jin, B. & DeNardo, L. A. Linking mPFC circuit maturation to the developmental regulation of emotional memory and cognitive flexibility. *Elife* **10**, (2021).
17. Hodel, A. S. Rapid infant prefrontal cortex development and sensitivity to early environmental experience. *Developmental Review* **48**, 113–144 (2018).
18. Rubenstein, J. L. R. & Merzenich, M. M. Model of autism: increased ratio of excitation/inhibition in key neural systems. *Genes Brain Behav* **2**, 255–267 (2003).
19. del Pino, I., Rico, B. & Marín, O. Neural circuit dysfunction in mouse models of neurodevelopmental disorders. *Current Opinion in Neurobiology* Preprint at https://doi.org/10.1016/j.conb.2017.12.013 (2018).
20. Zhao, H. *et al.* GABAergic System Dysfunction in Autism Spectrum Disorders. *Front Cell Dev Biol* **9**, (2022).
21. Schwede, M. *et al.* Strong correlation of downregulated genes related to synaptic transmission and mitochondria in post-mortem autism cerebral cortex. *J Neurodev Disord* **10**, 1–9 (2018).

22. Parikshak, N. N. *et al.* Integrative functional genomic analyses implicate specific molecular pathways and circuits in autism. *Cell* (2013) doi:10.1016/j.cell.2013.10.031.
23. Ariza, J., Rogers, H., Hashemi, E., Noctor, S. C. & Martínez-Cerdeño, V. The Number of Chandelier and Basket Cells Are Differentially Decreased in Prefrontal Cortex in Autism. *Cerebral Cortex* **28**, 411–420 (2018).
24. Hashemi, E., Ariza, J., Rogers, H., Noctor, S. C. & Martínez-Cerdeño, V. The number of parvalbumin-expressing interneurons is decreased in the prefrontal cortex in autism. *Cerebral Cortex* **27**, 1931–1943 (2017).
25. Dufour, B. D., McBride, E., Bartley, T., Juarez, P. & Martínez-Cerdeño, V. Distinct patterns of GABAergic interneuron pathology in autism are associated with intellectual impairment and stereotypic behaviors. *Autism* **27**, 1730–1745 (2023).
26. Gogolla, N., Takesian, A. E., Feng, G., Fagiolini, M. & Hensch, T. K. Sensory Integration in Mouse Insular Cortex Reflects GABA Circuit Maturation. *Neuron* (2014) doi:10.1016/j.neuron.2014.06.033.
27. Orefice, L. L. *et al.* Targeting Peripheral Somatosensory Neurons to Improve Tactile-Related Phenotypes in ASD Models. *Cell* (2019) doi:10.1016/j.cell.2019.07.024.
28. Peñagarikano, O. *et al.* Absence of CNTNAP2 leads to epilepsy, neuronal migration abnormalities, and core autism-related deficits. *Cell* **147**, 235–246 (2011).
29. Vogt, D. *et al.* Mouse Cntnap2 and Human CNTNAP2 ASD Alleles Cell Autonomously Regulate PV + Cortical Interneurons. *Cerebral Cortex* **28**, 3868–3879 (2018).
30. Zhang, L. *et al.* Hyperactivated PTP1B phosphatase in parvalbumin neurons alters anterior cingulate inhibitory circuits and induces autism-like behaviors. *Nat Commun* **11**, 1–15 (2020).
31. Orefice, L. L. L. *et al.* Peripheral Mechanosensory Neuron Dysfunction Underlies Tactile and Behavioral Deficits in Mouse Models of ASDs. *Cell* (2016) doi:10.1016/j.cell.2016.05.033.
32. Filice, F., Vörckel, K. J., Sungur, A. Ö., Wöhr, M. & Schwaller, B. Reduction in parvalbumin expression not loss of the parvalbumin-expressing GABA interneuron subpopulation in genetic parvalbumin and shank mouse models of autism. *Mol Brain* (2016) doi:10.1186/s13041-016-0192-8.
33. Negwer, M. *et al.* EHMT1 regulates Parvalbumin-positive interneuron development and GABAergic input in sensory cortical areas. *Brain Struct Funct* **225**, 2701–2716 (2020).
34. Kalinowska, M. *et al.* Deletion of Fmr1 in parvalbumin-expressing neurons results in dysregulated translation and selective behavioral deficits associated with fragile X syndrome. *Mol Autism* **13**, 29 (2022).
35. Fishell, G. & Kepecs, A. Interneuron Types as Attractors and Controllers. *Annu Rev Neurosci* **43**, 1–30 (2020).
36. Tremblay, R., Lee, S. & Rudy, B. GABAergic Interneurons in the Neocortex: From Cellular Properties to Circuits. *Neuron* **91**, 260–292 (2016).
37. Hu, H., Gan, J. & Jonas, P. Fast-spiking, parvalbumin $^{+}$ GABAergic interneurons: From cellular design to microcircuit function. *Science (1979)* **345**, (2014).
38. Pinto, D. *et al.* Convergence of genes and cellular pathways dysregulated in autism spectrum disorders. *Am J Hum Genet* (2014) doi:10.1016/j.ajhg.2014.03.018.
39. Grove, J. *et al.* Identification of common genetic risk variants for autism spectrum disorder. *Nat Genet* **51**, 431–444 (2019).
40. Satterstrom, F. K. *et al.* Large-Scale Exome Sequencing Study Implicates Both Developmental and Functional Changes in the Neurobiology of Autism. *SSRN Electronic Journal* (2019) doi:10.2139/ssrn.3371405.
41. Contractor, A., Ethell, I. M. & Portera-Cailliau, C. Cortical interneurons in autism. *Nat Neurosci* **24**, 1648–1659 (2021).

42. De Rubeis, S. *et al.* Delineation of the genetic and clinical spectrum of Phelan-McDermid syndrome caused by SHANK3 point mutations. *Mol Autism* (2018) doi:10.1186/s13229-018-0205-9.
43. Leblond, C. S. *et al.* Meta-analysis of SHANK Mutations in Autism Spectrum Disorders: A Gradient of Severity in Cognitive Impairments. *PLoS Genet* (2014) doi:10.1371/journal.pgen.1004580.
44. Jiang, Y. hui & Ehlers, M. D. Modeling Autism by SHANK Gene Mutations in Mice. *Neuron* vol. 78 8–27 Preprint at https://doi.org/10.1016/j.neuron.2013.03.016 (2013).
45. Yi, F. *et al.* Autism-associated SHANK3 haploinsufficiency causes Ih channelopathy in human neurons. *Science* (2016) doi:10.1126/science.aaf2669.
46. Zhu, M. *et al.* Shank3-deficient thalamocortical neurons show HCN channelopathy and alterations in intrinsic electrical properties. *J Physiol* **596**, 1259–1276 (2018).
47. Wang, W. *et al.* Striatopallidal dysfunction underlies repetitive behavior in Shank3-deficient model of autism. *Journal of Clinical Investigation* (2017) doi:10.1172/JCI87997.
48. Guo, B. *et al.* Restoring thalamocortical circuit dysfunction by correcting HCN channelopathy in Shank3 mutant mice. *Cell Rep Med* **5**, 101534 (2024).
49. Wang, X. *et al.* Altered mGluR5-Homer scaffolds and corticostriatal connectivity in a Shank3 complete knockout model of autism. *Nat Commun* **7**, 11459 (2016).
50. Mei, Y. *et al.* Adult restoration of Shank3 expression rescues selective autistic-like phenotypes. *Nature* **530**, 481–4 (2016).
51. Dhamne, S. C. *et al.* Replicable in vivo physiological and behavioral phenotypes of the Shank3B null mutant mouse model of autism. *Mol Autism* (2017) doi:10.1186/s13229-017-0142-z.
52. Pagani, M. *et al.* Deletion of autism risk gene shank3 disrupts prefrontal connectivity. *Journal of Neuroscience* (2019) doi:10.1523/JNEUROSCI.2529-18.2019.
53. Guo, B. *et al.* Anterior cingulate cortex dysfunction underlies social deficits in Shank3 mutant mice. *Nat Neurosci* (2019) doi:10.1038/s41593-019-0445-9.
54. Chen, Q. *et al.* Dysfunction of cortical GABAergic neurons leads to sensory hyper-reactivity in a Shank3 mouse model of ASD. *Nat Neurosci* **23**, 520–532 (2020).
55. Patz, S., Grabert, J., Gorba, T., Wirth, M. J. & Wahle, P. Parvalbumin Expression in Visual Cortical Interneurons Depends on Neuronal Activity and TrkB Ligands during An Early Period of Postnatal Development. *Cerebral Cortex* **14**, 342–351 (2004).
56. Turner, K. C., Frost, L., Linsenbardt, D., McIlroy, J. R. & Müller, R.-A. Atypically diffuse functional connectivity between caudate nuclei and cerebral cortex in autism. *Behav Brain Funct* **2**, 34 (2006).
57. Willsey, A. J. *et al.* XCoexpression networks implicate human midfetal deep cortical projection neurons in the pathogenesis of autism. *Cell* (2013) doi:10.1016/j.cell.2013.10.020.
58. Wolff, J. J. *et al.* Differences in white matter fiber tract development present from 6 to 24 months in infants with autism. *American Journal of Psychiatry* (2012) doi:10.1176/appi.ajp.2011.11091447.
59. Hazlett, H. C. *et al.* Early brain development in infants at high risk for autism spectrum disorder. *Nature* (2017) doi:10.1038/nature21369.
60. Kabitzke, P. *et al.* Comprehensive Analysis of Two *Shank3* and the Cacna1c Mouse Models of Autism Spectrum Disorder. *Genes Brain Behav* (2017) doi:10.1111/gbb.12405.
61. Peixoto, R. T. *et al.* Abnormal Striatal Development Underlies the Early Onset of Behavioral Deficits in Shank3B−/− Mice. *Cell Rep* (2019) doi:10.1016/j.celrep.2019.10.021.
62. Vormstein-Schneider, D. *et al.* Viral manipulation of functionally distinct interneurons in mice, non-human primates and humans. *Nat Neurosci* **23**, 1629–1636 (2020).

63. Delevich, K., Tucciarone, J., Huang, Z. J. & Li, B. The mediodorsal thalamus drives feedforward inhibition in the anterior cingulate cortex via parvalbumin interneurons. *Journal of Neuroscience* **35**, 5743–5753 (2015).
64. Pachitariu, M. *et al.* Suite2p: beyond 10,000 neurons with standard two-photon microscopy. *bioRxiv* 061507 (2016) doi:10.1101/061507.
65. Stringer, C., Wang, T., Michaelos, M. & Pachitariu, M. Cellpose: a generalist algorithm for cellular segmentation. *Nat Methods* **18**, 100–106 (2021).
66. Lee, E. *et al.* Excitatory synapses and gap junctions cooperate to improve Pv neuronal burst firing and cortical social cognition in Shank2-mutant mice. *Nat Commun* **12**, 5116 (2021).
67. Bartos, M., Vida, I. & Jonas, P. Synaptic mechanisms of synchronized gamma oscillations in inhibitory interneuron networks. *Nat Rev Neurosci* **8**, 45–56 (2007).
68. Roth, F. C. & Hu, H. An axon-specific expression of HCN channels catalyzes fast action potential signaling in GABAergic interneurons. *Nat Commun* **11**, 2248 (2020).
69. Miyamae, T., Chen, K., Lewis, D. A. & Gonzalez-Burgos, G. Distinct physiological maturation of parvalbumin-positive neuron subtypes in mouse prefrontal cortex. *Journal of Neuroscience* **37**, 4883–4902 (2017).
70. Pagano, J. *et al.* Shank3 deletion in PV neurons is associated with abnormal behaviors and neuronal functions that are rescued by increasing GABAergic signaling. *Mol Autism* **14**, 28 (2023).
71. Bey, A. L. *et al.* Brain region-specific disruption of Shank3 in mice reveals a dissociation for cortical and striatal circuits in autism-related behaviors. *Transl Psychiatry* **8**, 94 (2018).
72. Ali, F. *et al.* Inhibitory regulation of calcium transients in prefrontal dendritic spines is compromised by a nonsense Shank3 mutation. *Mol Psychiatry* **26**, 1945–1966 (2021).
73. Peixoto, R. T. *et al.* Early hyperactivity and precocious maturation of corticostriatal circuits in Shank3B-/- mice. *Nat Neurosci* **19**, 716–24 (2016).
74. Ortiz-Cruz, C. A., Marquez, E. J., Linares-García, C. I., Perera-Murcia, G. R. & Ramiro-Cortés, Y. Haploinsufficiency of Shank3 increases the orientation selectivity of V1 neurons. *Sci Rep* **12**, 22230 (2022).
75. Kim, S. *et al.* Neural circuit pathology driven by Shank3 mutation disrupts social behaviors. *Cell Rep* **39**, 110906 (2022).
76. Yildiz, B. *et al.* Shank3 related muscular hypotonia is accompanied by increased intracellular calcium concentrations and ion channel dysregulation in striated muscle tissue. *Front Cell Dev Biol* **11**, (2023).
77. Kim, Y. *et al.* The emerging roles of Shank3 in cardiac function and dysfunction. *Front Cell Dev Biol* **11**, (2023).
78. Perfitt, T. L. *et al.* Neuronal L-Type Calcium Channel Signaling to the Nucleus Requires a Novel CaMKIIα-Shank3 Interaction. *The Journal of Neuroscience* **40**, 2000–2014 (2020).
79. Yang, Q. *et al.* Clustering of <scp> Ca $_{V}$ 1 </scp> .3 L-type calcium channels by Shank3. *J Neurochem* **167**, 16–37 (2023).
80. Kolevzon, A., Delaby, E., Berry-Kravis, E., Buxbaum, J. D. & Betancur, C. Neuropsychiatric decompensation in adolescents and adults with Phelan-McDermid syndrome: A systematic review of the literature. *Molecular Autism* Preprint at https://doi.org/10.1186/s13229-019-0291-3 (2019).
81. Han, S., Tai, C., Jones, C. J., Scheuer, T. & Catterall, W. A. Enhancement of inhibitory neurotransmission by GABAA receptors having α2,3-subunits ameliorates behavioral deficits in a mouse model of autism. *Neuron* **81**, 1282–1289 (2014).
82. Han, S. *et al.* Autistic-like behaviour in Scn1a +- mice and rescue by enhanced GABA-mediated neurotransmission. *Nature* **489**, 385–390 (2012).
83. Kourdougli, N. *et al.* Improvement of sensory deficits in fragile X mice by increasing cortical interneuron activity after the critical period. *Neuron* **111**, 2863-2880.e6 (2023).

84. El-Hassar, L. *et al.* Modulators of Kv3 Potassium Channels Rescue the Auditory Function of Fragile X Mice. *The Journal of Neuroscience* **39**, 4797–4813 (2019).